6-1-1998

Permitted Iron Emission Lines in the Classical T Tauri Star DR Tauri

Georgina Beristain
Smith College

Suzan Edwards
Smith College, sedwards@smith.edu

John Kwan
University of Massachusetts Amherst

Recommended Citation

Beristain, Georgina; Edwards, Suzan; and Kwan, John, "Permitted Iron Emission Lines in the Classical T Tauri Star DR Tauri" (1998). Astronomy: Faculty Publications, Smith College, Northampton, MA.
https://scholarworks.smith.edu/ast_facpubs/14

THE ASTROPHYSICAL JOURNAL, 499:828–852, 1998 June 1

PERMITTED IRON EMISSION LINES IN THE CLASSICAL T TAURI STAR DR TAURI

GEORGINA BERISTAIN,[1,2] SUZAN EDWARDS,[2,3] AND JOHN KWAN[1]

Received 1997 September 11; accepted 1998 January 7

ABSTRACT

We present a study of permitted emission lines of Fe I and Fe II in the spectrum of the high–accretion rate classical T Tauri star DR Tau. Echelle spectra collected at the 4 m Mayall telescope at Kitt Peak National Observatory between 1988 and 1992 include four epochs with red spectral coverage (~5000–6800 Å) and three with blue spectral coverage (~4000–4950 Å). A total of 62 unblended Fe I and Fe II lines are identified, their profiles are examined, and ratios of line pairs that are sensitive to column density or temperature are analyzed.

The unblended Fe profiles exhibit a systematic behavior, with FWHM increasing from 20 to between 70 and 90 km s^{-1} as the equivalent width increases from 0.05 to several Å. Two-component fits to the profiles suggest a composite origin, comprising a narrow component (NC), with FWHM ~ 20 km s^{-1} and a radial velocity at rest with respect to the photosphere, and a broad component (BC), with FWHM ~ 100 km s^{-1} and a tendency to be blueshifted by ≤ 10 km s^{-1}. These two kinematic components are present in differing proportions among lines of differing intensity, thereby accounting for the systematic behavior of the profiles with line strength.

Estimates of opacities and column densities are obtained by comparing observed intensity ratios of lines from a common upper level with values expected from a local escape probability calculation. We find that (1) opacities in the NC exceed those in the BC by factors of 2–4 and (2), for the BC, $N_{\rm Fe\,I} \gtrsim 10^{17}$–$10^{18}$ cm^{-2} and $N_{\rm Fe\,II} \gtrsim 10^{18}$–$10^{19}$ cm^{-2} for kinetic temperatures in the range 4000–10,000 K. Ratios of NC-to-BC emission from a pair of Fe I lines that are insensitive to opacity suggest that the kinetic temperature in the NC exceeds that in the BC by several thousand degrees.

The centroid velocity and width of the NC in Fe I and Fe II are comparable to those from photospheric lines, suggesting a thermal or turbulent origin further broadened by stellar rotation. In the context of a magnetospheric accretion model, the NC is consistent with an origin in the postshock gas close to the stellar surface. In contrast, the BC is likely to be broadened by bulk motion, such as infalling gas in the accretion funnel or rotation in the region coupling the inner disk to the stellar magnetic field.

Subject headings: accretion, accretion disks — line: profiles — stars: emission-line, Be — stars: pre–main-sequence

1. INTRODUCTION

The permitted emission lines in the spectra of classical T Tauri stars (cTTS's) contain a wealth of untapped information on the complex region where the stellar magnetosphere interacts with the accretion disk. Historically one of the defining characteristics of a cTTS is a distinctive set of optical emission lines, cited as resembling the spectrum of the solar chromosphere (Joy 1945; Herbig 1962). The most prominent lines are from the hydrogen Balmer series and Ca II H and K, accompanied by a rich array of metallic features including permitted lines of Fe I, Fe II, He I, He II, Ti II, Na I, and Ca I, plus forbidden lines of [O I], [S II], and [N II]. In the last decade, studies of the Balmer and forbidden lines have elucidated some of the kinematic activity in these accretion disk systems.

The Balmer profiles in cTTS's suggest the presence of magnetic funnel flows, created as the stellar magnetosphere truncates the inner disk and redirects the accretion flow along magnetic trajectories terminating in accretion shocks on the stellar surface (Bertout 1989; Königl 1991; Edwards et al. 1994, hereafter EHGA; Hartmann, Hewett, & Calvet 1994, hereafter HHC; Muzerolle, Calvet, & Hartmann 1998, hereafter MCH). At the same time, the blueshifted absorption features commonly seen at Hα indicate high-speed winds that must originate from either the star or the very inner accretion disk. Within tens of AUs, the outflows become highly collimated into jets, which radiate in shock-excited forbidden lines (Kwan & Tademaru 1988; Hartigan, Edwards, & Ghandour 1995, hereafter HEG; Hirth, Mundt, & Solf 1997).

The stellar magnetosphere is also implicated in spinning down the central star, thereby accounting for the small angular velocities that characterize cTTS photospheres (Edwards et al. 1993; Bouvier et al. 1993, 1995). Together these phenomena have been interpreted as indicating that the stellar magnetosphere mediates the disk accretion process and plays a fundamental role in the angular momentum evolution of the star/disk system (Königl 1991; Ostriker & Shu 1995; Ghosh 1995; Li, Wickramasinghe, & Ruediger 1996; Armitage & Clarke 1996; Paatz & Camenzind 1996). Considerable ambiguity remains with this interpretation, however, where key unresolved issues include how the stellar magnetosphere is coupled to the disk, how stellar spin-down is achieved, and whether open field lines from the stellar magnetosphere or from a disk magnetosphere are the primary agent launching the outflows (Shu et al. 1994; Najita & Shu 1994; Camenzind 1997; Safier 1998).

---

[1] Five College Astronomy Department, University of Massachusetts, Amherst, MA 01003.

[2] Visiting Astronomer, Kitt Peak National Observatory, operated by the National Optical Astronomy Observatory under contract to the National Science Foundation.

[3] Five College Astronomy Department, Smith College, Northampton, MA 01063.

This is the first in a series of papers to examine the permitted metallic emission features in cTTS spectra. We anticipate providing additional insight into the complex star/disk interaction region, where the funnel flow and outflow presumably originate. In this work we examine the plethora of permitted Fe I and Fe II lines in the optical spectrum of one high–accretion rate star, DR Tau, with the goal of elucidating any systematic behavior of the line profiles and providing estimates of physical conditions, including optical depth, column density, and kinetic temperature, in the Fe line formation region.

Iron emission in cTTS's was first mentioned by Joy (1945), who noted the similarity to the solar chromospheric spectrum, which is dominated in the optical by Fe I lines. The complex term structure of the Fe atom because of the incomplete 3d shell and the mixing of states caused by the frequent departures from any pure coupling scheme conspire to produce a rich array of emission lines at ultraviolet, optical, and infrared wavelengths. In neutral and once-ionized iron, the large number of low-lying ($\lesssim 6$ eV), closely spaced ($\lesssim 0.05$ eV) energy levels within spectroscopic terms of alternating parity allows a large number of permitted transitions to be excited by collisions. This fact and the relatively low energy needed for collisional excitation make Fe I and Fe II emission an important cooling agent at low temperatures ($T \lesssim 10^4$ K).

The strength of Fe I (43) fluorescent emission led Herbig (1962) to include it as one of the defining characteristics of a cTTS. An early analysis of the fluorescent Fe lines identified Ca II H or Hϵ as the pumping transition and established the range of electron densities that favor fluorescent Fe emission in an optically thin envelope (Willson 1974, 1975). Later, the fluorescent Fe I lines in the cTTS RU Lup were used to estimate hydrogen and electron densities under LTE conditions with an escape probability approximation (Lago 1982).

While Fe emission is in principle a promising diagnostic of physical conditions and a potential probe of the inner disk environment, the study of iron in cTTS's is also beset with a number of difficulties that have hindered past investigators. Factors that complicate the analysis include the photospheric spectrum underlying the emission lines, the severity of line blending from neighboring metallic features, and the relative weakness of many of these lines. Furthermore, until recently, large uncertainties in atomic transition probabilities hampered detailed analyses of Fe in astrophysical spectra.

Many of these problems are surmounted in this investigation, in which we (1) use the most recent compilations of Fe transition probabilities, with uncertainties $\lesssim 10\%$ in Fe I and $\lesssim 25\%$ in Fe II (Nave et al. 1994; Giridhar & Arellano Ferro 1995); (2) employ high-resolution echelle spectra from the cTTS samples described in EHGA and HEG that have the stellar photospheric features and continuum veiling removed, leaving uncontaminated *residual* line profiles; and (3) focus on DR Tau, a cTTS that displays a rich metallic spectrum dominated by Fe I and Fe II lines but whose Fe lines are half as broad as those of other highly veiled objects in the spectroscopic sample, thereby minimizing blends due to overlapping line wings and allowing many more transitions to be analyzed. One drawback to the current data set is the nonsimultaneity of our three blue ($\sim \lambda\lambda 4000$–4950) and four red ($\sim \lambda\lambda 5000$–6800) spectra, so that some of the most potentially sensitive line ratio diagnostics cannot be employed. Nevertheless, we explore here the possibilities inherent in the study of Fe lines as diagnostics of cTTS accretion and urge that new data be obtained that will fully utilize the information available from these lines.

The star selected for the first phase of this study, DR Tau, is one of the brightest and most frequently observed cTTS's. Its optical continuum veiling, which is attributed to luminosity from an accretion shock at the stellar surface, is large and variable, with values in the literature ranging from ~ 0.7 to 20 times the stellar continuum flux (Basri & Batalha 1990; Guenther & Hessman 1993; HEG; Hessman & Guenther 1997). Corresponding mass accretion rates are somewhat uncertain because of the difficulty in assessing the extinction to this source and its significant variability, but are always at the high end of accretion rates derived for cTTS's, with estimates ranging from $\dot{M}_{\rm acc} \sim 10^{-7}$ to 10^{-5} $M_\odot$ yr^{-1} (Bertout, Basri, & Bouvier 1988; Basri & Bertout 1989; Kenyon et al. 1994; HEG). Spectroscopic evidence for magnetospheric funnel flows, in the form of inverse P Cygni profiles in upper Balmer lines, Na D, He I, and Fe II are also commonly reported in studies of DR Tau (Bertout et al. 1977; Appenzeller et al. 1980; Krautter & Bastian 1980; Guenther & Hessman 1993; EHGA; HHC; Smith et al. 1997). Additionally, the near-infrared spectral energy distribution of DR Tau was one of the earliest cTTS's to be modeled by a magnetospherically truncated inner disk, with a hole size of $\sim 5 R_*$ (Bertout et al. 1988; Kenyon et al. 1994).

This paper is organized as follows: the spectroscopic data for DR Tau and the identification of 62 unblended Fe I and Fe II lines are presented in § 2. An empirical examination of the unblended Fe profiles is presented in § 3, elucidating the basic kinematics of the Fe line formation region. Pairs of lines that share common upper levels are identified in § 4 and used to derive physical conditions via application of an escape probability analysis. A discussion of the results is presented in § 5, and the conclusions are presented in § 6.

2. THE SPECTRA

The seven echelle spectra of DR Tau used for this study are taken from a data set that was the basis for two previous publications focused on Balmer and forbidden lines in 32 cTTS's and 10 weak-emission T Tauri stars (EHGA; HEG). All spectra were taken with the 4 m Mayall telescope at Kitt Peak National Observatory (KPNO) with a velocity resolution of ~ 12 km s^{-1}. The spectra cover two wavelength regions, which are taken nonsimultaneously; the four red spectra were obtained on 1988 January 7 and 10, 1988 November 30, and 1990 January 17 with a wavelength coverage from $\lambda\lambda 5000$–6800, and the three blue spectra were obtained on 1988 November 20 and 1992 December 1 and 2 with a wavelength coverage from $\lambda\lambda 4000$–4950. The grating settings vary somewhat among the runs and are tabulated explicitly in Table 1. The data reduction for these spectra, including evaluation of the residual emission line profiles and determination of the veiling, is fully described in the two previously published papers.

Determination of the *residual* emission line profiles begins with the selection of a photospheric template of similar spectral type (K7/M0 for DR Tau), and the cTTS spectrum is then simulated by adding a constant monochromatic flux to the template over a small (about 80 Å) region, until the depths of the artificially veiled photospheric features match those of the T Tauri star. Residual

TABLE 1

DR TAU SPECTRA

VEILING	HJD 2,440,000+	λ RANGE (Å)	STRONGEST MULTIPLETS OBSERVED Fe I	STRONGEST MULTIPLETS OBSERVED Fe II
		r_R		
20	7170.7	5128–6760	15, 37, 168, 169, 686	46, 48, 49, 55, 74
10	7167.8	5130–6760	15, 37, 168, 169, 686	46, 48, 49, 55, 74
9	7908.8	5272–6760	15, 37, 168, 169, 686	46, 48, 49, 55, 74
6	7495.9	4985–6806	15, 37, 168, 169, 686	42, 46, 48, 49, 55, 74
		r_B		
13	8958.8	4023–4970	2, 41, 42, 43, 68	27, 28, 37, 38, 42
9	7485.8	3985–4920	2, 41, 42, 43, 68	27, 28, 37, 38
8	8959.8	4020–4970	2, 41, 42, 43, 68	27, 28, 37, 38, 42

profiles result from the subtraction of the artificially veiled template from the observed T Tauri star spectrum, revealing emission lines free of distortion by the underlying photosphere. This procedure gives unprecedented sensitivity in defining weak emission features in T Tauri spectra, allowing us to study Fe line profiles with equivalent widths as low as 0.1 Å. The weakest lines measurable in the spectra depend on the signal-to-noise ratio (S/N), which ranges from 50 to 75 in the continuum, with resultant detection limits in equivalent width of ~0.02–0.05 Å.

The optical continuum veiling flux is also determined by this procedure. It is parameterized by r_λ, the ratio of veiling emission to photospheric radiation at $\lambda = 5700$ (r_R) for our red spectra and at $\lambda = 4500$ (r_B) for our blue spectra. Measured veilings for the seven spectra studied here are in the ranges $6 \leq r_R \leq 20$ and $8 \leq r_B \leq 13$ and were originally reported in EHGA and HEG. Table 1 identifies the date and corresponding veiling for each observation of DR Tau; throughout the paper, we refer to each spectrum by r_λ rather than the date, since the time coverage is infrequent and intermittent.

2.1. *Identification of Unblended Iron Lines*

The strongest lines in our optical spectra of DR Tau are from the hydrogen Balmer series, with equivalent widths 1.5–2 orders of magnitude larger than those of other lines. After Hα, the next strongest lines in the red spectra are from He I λ5876 and λ6678. Then follow Fe II (42), the Mg I (2) triplet and the Na I doublet, and [O I] λ6300. The red spectra also include numerous lines of Fe II and Fe I, plus [O I] λ5577 and other forbidden lines from [S II] and [N II]. In the blue spectra, after the Balmer lines, Fe II (42) are the strongest features, followed by numerous lines of Fe II and Fe I, He I, Ti II, Cr II, Ni I, and He II. The most abundant optical features, however, are from Fe. The optical Fe lines share upper levels with many UV lines, which are expected to be very strong. As a group the Fe lines likely constitute an important coolant in cTTS's.

The total number of Fe lines we identified in DR Tau is approximately 150, with 70 Fe I and 30 Fe II transitions identified in the red and 27 Fe I and 25 Fe II lines in the blue. No Fe III or forbidden line transitions are observed.

The full suite of ~150 Fe I and Fe II lines are characterized as follows:

1. Fe I lines in the red spectra arise from 14 multiplets (1, 15, 16, 36, 37, 62, 66, 111, 168, 169, 207, 268, 686, and 816) spanning excitation energies that range from 2.4 to 5.6 eV above ground. Most concentrate in three clusters at ~3.3, 4.4, and 5.6 eV. The largest oscillator strengths are from transitions in multiplets 686 and 816 with Einstein $A_{ij} \sim 10^7$–10^8 s^{-1}.
2. Fe I lines in the blue spectra arise from six multiplets (2, 39, 41, 42, 43, and 68) with excitation energies between 2.8 and 5.0 eV above ground. Again, most concentrate in three clusters at 2.8, 4.4, and 5.0 eV. The largest oscillator strengths are from transitions in multiplets 41, 42, and 43, with A_{ij} values of ~ 10^7 s^{-1}.
3. Fe II lines in the red spectra arise from eight multiplets (40, 41, 42, 46, 48, 49, 55, and 74) with upper levels at energies between 4.8 and 5.8 eV above ground. Among them the strongest transitions occur in multiplets 42 and 49, with A_{ij} of 10^6–10^7 s^{-1}.
4. Fe II lines in the blue spectra arise from five multiplets (27, 28, 37, 38, and 42) with upper levels at energies 5.4 and 5.6 eV above ground. The strongest transitions are found in multiplets 27, 38, and 42 with A_{ij} values of 10^6–10^7 s^{-1}.
5. The majority of the observed Fe I transitions decay to metastable levels between 0.0 and 2.6 eV, except for those from multiplets 686 and 816, which decay to nonmetastable levels between 3.3 and 3.7 eV above ground.
6. The Fe II lines decay to metastable levels between 2.6 and 3.9 eV above ground.

Unfortunately the majority of the ~150 Fe lines in our spectra are blended with neighboring features, rendering them ineffective as probes of the kinematic and physical conditions in DR Tau's Fe line formation region. After careful examination, we identified a total of 62 unblended Fe lines for further study; they are listed in Tables 2 and 3. The identification of blends is straightforward when the overlapping transition is resolved, in which case the resultant distorted profiles are readily distinguished. The identification of unresolved blends is more laborious, and requires use of the solar photospheric spectrum as a reference (Moore, Minnaert, & Houtgast 1966). Additional transitions from the parent multiplet of the suspected blending line can be found from the solar spectrum and those with comparable or larger A_{ij} as the suspected blend are used to estimate the blend's relative contribution in the cTTS spectrum. If such transitions are too weak to be detectable in the cTTS spectrum, the blend contribution is deemed to be unimportant. The most common blends, in order of decreasing incidence, are due to Fe I, Fe II, Ti II, Cr II, Ti I, Cr I, and Ni I.

TABLE 2

Unblended Fe i Lines in DR Tau

				W_λ (Å)			
Multiplet	λ Å	E_u (eV)	$\log A_{ij}$ (s^{-1})	$r_R = 6$ or $r_B = 8$	$r_R = 9$ or $r_B = 9$	$r_R = 10$ or $r_B = 13$	$r_R = 20$ $r_R = 20$
$a\,^5D$–$z\,^7F^o$ (2).........	4375.93**	2.83	4.47	0.25	0.59	0.16	
$a\,^3F$–$z\,^5D^o$ (15)	5371.49*	3.27	6.02	0.11	0.20	0.30	0.22
	5405.77	3.28	6.00	0.09	0.14	0.21	0.13
	5455.61	3.28	5.78	0.10	0.10	0.19	0.10
	5429.70*	3.24	5.63	0.12	0.21	0.36	0.23
	5397.13*	3.21	5.41	0.11	0.18	0.30	0.15
	5497.52*	3.27	4.80	0.06	0.07	0.09	0.05
	5506.78*	3.24	4.70	0.05	0.07	0.09	0.04
	5501.46*	3.21	4.43	0.05	0.06	0.07	0.04
$a\,^5F$–$z\,^5F^o$ (16)	5083.34	3.40	4.75	<0.03	...	...	...
	5051.63	3.37	4.71	0.04	...	...	...
	5151.91	3.42	4.38	<0.02	...	0.03	<0.01
	5142.93	3.37	4.37	<0.02	...	...	...
$a\,^3F$–$z\,^3D^o$ (37)	5341.02	3.93	5.72	0.07	0.11	0.18	0.08
$a\,^3F$–$y\,^5F^o$ (39)	4531.15	4.22	5.40	0.02	0.09	<0.01	
$a\,^3F$–$z\,^5G^o$ (41)	4404.75	4.37	7.48	0.39	1.30	0.35	
$a\,^3F$–$z\,^3G^o$ (42)	4250.79	4.47	7.18	0.06	0.36	0.14	
	4202.03	4.43	6.91	0.20	0.52	0.14	
$a\,^3F$–$z\,^3F^o$ (43)	4045.81	4.55	7.94	0.28	0.78	0.21	
	4063.59*	4.61	7.82	0.90	3.27	0.69	
	4132.06*	4.61	7.07	0.38	1.35	0.26	
$a\,^3P$–$y\,^5D^o$ (62)	6335.34	4.15	5.15	0.02	0.04	0.06	0.04
	6219.28	4.19	5.10	0.04	0.05	0.04	0.02
	6265.13	4.15	4.84	<0.01	<0.01	0.02	0.03
$a\,^5P$–$x\,^5D^o$ (68)	4494.56	4.96	6.54	0.03	0.20	0.02	
$a\,^3P$–$z\,^3P^o$ (111)	6663.45	4.28	5.72	...	<0.02	<0.02	0.02
	6421.35	4.21	5.57	0.03	<0.04	0.04	0.02
$a\,^3H$–$z\,^5G^o$ (168)......	6494.98*	4.31	5.88	0.03	0.07	0.10	0.07
	6393.60	4.37	5.83	0.03	0.03	0.07	0.05
	6593.88*	4.31	4.72	<0.02	<0.06	0.03	<0.04
$a\,^3H$–$z\,^3G^o$ (169)......	6191.56	4.43	5.94	0.03	0.08	0.12	0.08
	6252.55	4.39	5.50	<0.01	0.03	0.03	0.04
$b\,^3F$–$y\,^3F^o$ (207)	6065.48	4.65	6.03	0.01	<0.01	0.02	0.02
	6230.73	4.55	6.00	0.03	0.04	0.06	0.05
	6200.32	4.61	4.96	<0.01	<0.01	<0.01	<0.01
$a\,^3G$–$y\,^3F^o$ (268)	6592.91	4.61	5.87	<0.05	<0.09	0.12	<0.08
$z\,^5F^o$–$e\,^5D$ (686)	5615.64**	5.54	7.42	0.02	0.07	0.09	0.06
	5572.84	5.62	7.36	0.02	0.02	0.03	0.02
	5569.62	5.64	7.32	<0.01	0.01	0.02	0.03
	5624.54	5.62	6.87	<0.01	<0.01	<0.01	0.02
	5709.38	5.54	6.33	<0.02	<0.02	0.05	0.02
$z\,^5P^o$–$e\,^5D$ (816)	6400.00	5.54	6.97	0.03	0.04	0.06	0.06
	6411.65	5.59	6.77	<0.02	<0.02	0.02	0.02
	6408.02	5.62	6.49	<0.01	<0.01	<0.01	0.02

Note.—There are four entries for W_λ from the red spectra and three from the blue spectra. Each spectrum is identified by its veiling state, either r_R or r_B. The grating settings for each observing epoch differ somewhat, so that some lines are observable at one epoch but not another, as indicated by the ellipses. Lines comprising common upper level line pairs used in the LVG analysis for opacity and column density estimates are marked with single asterisks; the two opacity insensitive lines used to estimate kinetic temperatures are marked with double asterisks. Atomic parameter data for Fe i come from Kock, Kroll, & Schnehage 1984; Fuhr, Martin, & Wiese 1988; Bard, Kock, & Kock 1991; O'Brian et al. 1991; and Nave et al. 1994.

The final identification of 62 unblended Fe features include 35 red Fe i lines (from multiplets 15, 16, 37, 62, 111, 168, 169, 207, 268, 686, and 816), nine red Fe ii lines (from multiplets 42, 46, 48, 49, 55, and 74), nine blue Fe i lines (from multiplets 2, 39, 41, 42, 43, and 68) and nine blue Fe ii lines (from multiplets 27, 37, 38, and 42). The 62 unblended lines are tabulated in Tables 2 and 3, along with their atomic parameters and observed emission equivalent widths. These unblended lines still include a wide range of Einstein A_{ij} values and excitation potentials, and will form the basis for the rest of this paper.

2.2. *Comparison with Other Line Profiles*

It is informative to compare the profiles of the Fe lines with those exhibited by other strong emission features at the same epoch. Figure 1 presents simultaneous profiles of Hα, He i λ5876, Fe ii (49) λ5276, and Fe i (15) λ5397 from the red spectra; Figure 2 presents simultaneous profiles of Hβ, Hγ, Fe ii (37) λ4629, and Fe i (43) λ4064 from the blue spectra.

The Balmer lines, some of which appear in EHGA, are typical of those observed in DR Tau (Krautter & Bastian 1980; Hartmann 1982; Mundt 1984; Aiad et al. 1984; Appenzeller, Reitermann, & Stahl 1988; Isobe, Norimoto, & Kitamura 1988; Hessman & Guenther 1997). They are characterized by broad wings (± 500 km s^{-1}), blueshifted absorption features arising in outflowing gas, and occasional inverse P Cygni (IPC) structure in the upper Balmer lines arising in infalling gas, presumably in the magnetic funnel flow. A deep central absorption feature, whose

TABLE 3

UNBLENDED Fe II LINES IN DR TAU

MULTIPLET	(Å)	λ (eV)	E_u (s^{-1})	log A_{ij} or $r_B = 8$	$r_R = 6$ or $r_B = 9$	$r_R = 9$ or $r_B = 13$	$r_R = 10$ $r_R = 20$
				W_λ (Å)			
$b\,^4P$–$z\,^4D^o$ (27)......	4351.76*	5.55	5.67	0.62	2.61	0.85	
$b\,^4F$–$z\,^4F^o$ (37)......	4555.89	5.55	5.32	0.25	1.51	0.37	
	4515.34	5.59	5.32	0.47	1.11	0.20	
	4629.34	5.48	5.16	0.57	1.67	0.56	
	4520.23	5.55	4.93	0.17	0.69	0.28	
$b\,^4F$–$z\,^4D^o$ (38)......	4522.63	5.58	5.88	0.40	1.56	0.31	
	4508.28	5.61	5.83	0.40	1.22	0.31	
	4576.33*	5.55	4.79	0.06	0.41	0.12	
$a\,^6S$–$z\,^6P^o$ (42)	4923.93	5.41	6.60	1.59	...	1.35	
	5018.45	5.36	6.40	1.52	...	...	...
$a\,^4G$–$z\,^6F^o$ (46)......	5991.37	5.22	3.63	<0.03	0.04	0.11	0.09
	6084.10	5.24	3.48	<0.06	<0.03	0.05	0.05
$a\,^4G$–$z\,^4D^o$ (48)......	5362.86	5.49	4.85	0.23	0.31	0.44	0.30
$a\,^4G$–$z\,^4F^o$ (49)......	5276.00	5.55	5.53	0.49	0.66	0.97	0.80
	5197.56	5.62	5.69	0.33	...	0.74	0.50
	5234.62	5.59	5.36	0.48	...	0.95	0.62
$b\,^2H$–$z\,^4F^o$ (55)......	5534.83	5.48	4.57	0.21	0.23	0.39	0.27
$b\,^4D$–$z\,^4P^o$ (74)......	6456.39	5.82	5.23	0.21	0.33	0.57	0.38

NOTE.—See comments for Table 2. Atomic parameter data for Fe II come from Fuhr et al. 1988; Heise & Kock 1990; and Giridhar & Arellano Ferro 1995.

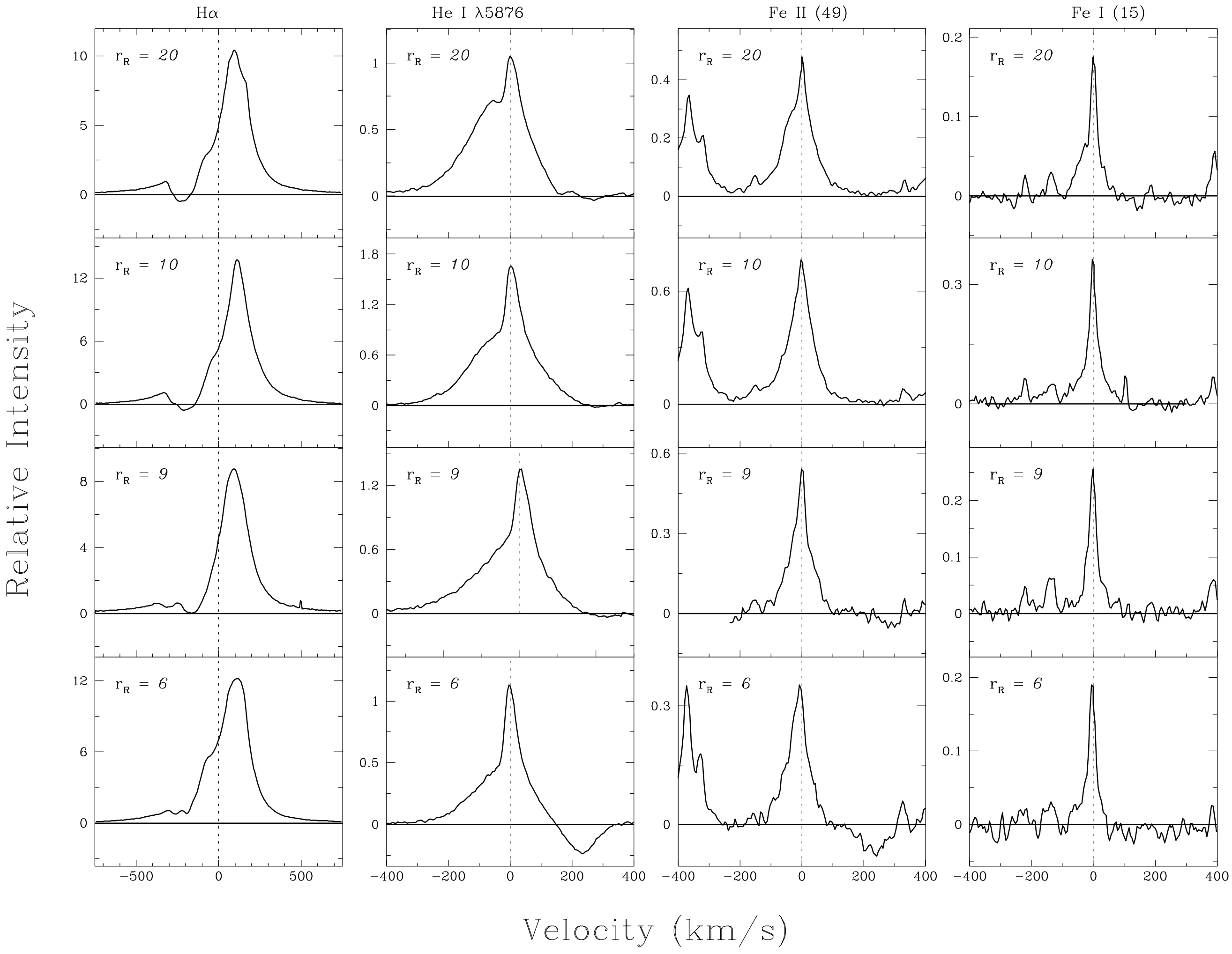

FIG. 1.—Residual emission profiles are shown for Hα, He I λ5876, Fe II (49) λ5276, and Fe I (15) λ5397 for the four red observing epochs, ordered by the magnitude of the veiling at λ5700, r_R. The velocity scale for the Balmer lines is almost twice that for the other lines. The ordinate is in units of the continuum flux and the velocity is measured relative to the photosphere.

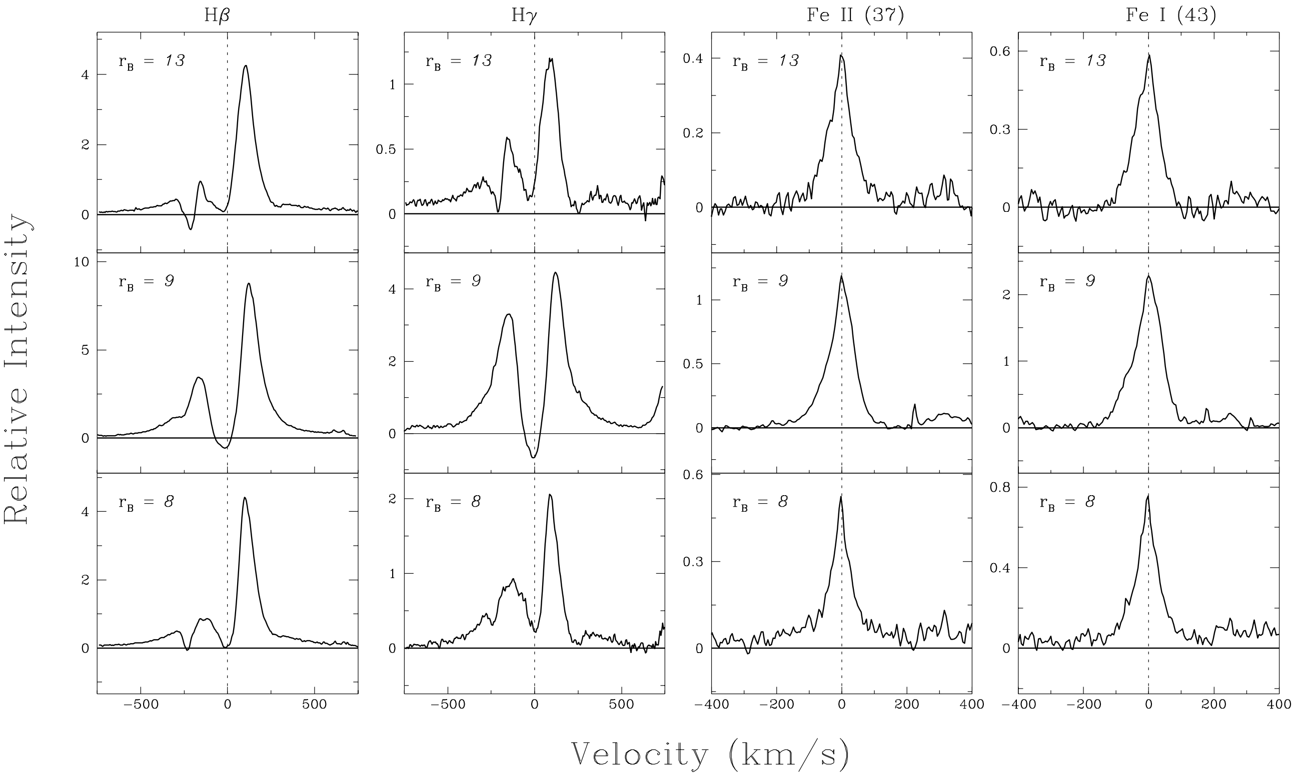

FIG. 2.—Residual emission profiles are shown for Hβ, Hγ, Fe II (37) λ4629, and Fe I (43) λ4064 for the three blue observing epochs, ordered by the magnitude of the veiling at λ4500, r_B. The velocity scale for the Balmer lines is almost twice that for the other lines. The ordinate is in units of the continuum flux and the velocity is measured relative to the photosphere.

origin is not yet known, is also prominent in the upper Balmer series (see Kwan 1997 for recent thoughts on this component).

In contrast to the hydrogen lines, the helium and other metallic profiles in DR Tau are several hundred km s^{-1} narrower than the Balmer lines, and they lack the multiple absorption components (note a factor of 2 change in velocity scale between the Balmer and metallic lines in Figs. 1 and 2). However, the metallic lines themselves display an array of profile types, most notably a variety of line widths, as illustrated by the decreasing widths from He I λ5876 to Fe II (49) λ5276 to Fe I (15) λ5397 in Figure 1. Several authors have characterized the metallic profiles as composite, consisting of a narrow central peak (the narrow component NC) and a broad pedestal (the broad component BC; Appenzeller et al. 1988; Hamman & Persson 1992; Batalha et al. 1996; Edwards 1997). In some lines, such as He I, these two components are quite distinctive, but in others, such as Fe I, they can combine to produce a triangular profile.

We observe IPC structure in several metallic lines in one of our red epochs and in two of our blue ones. In the red, at the lowest veiling state, $r_R = 6$, IPC features are seen in He I, Mg I, Na I, and the strongest lines of Fe II (multiplets 42, 48, and 49). In the blue, at $r_B = 8$ and 13, IPC structure is observed in the upper Balmer and the strongest Fe II lines (multiplets 27, 38, and 42; not shown in Fig. 2). The vast majority of the Fe emission lines do not show redshifted absorption features, although the broad component is often slightly blueshifted, as would be expected from magnetospheric infall.

In order to interpret the metallic line profiles in cTTS spectra, it is imperative to quantify their morphology and to determine whether the apparent composite structure of these lines arises in two distinct regions, as suggested by Hamman & Persson (1992) and Batalha et al. (1996), or whether the profiles result from the geometrical projection of velocity vectors from a single region, such as a funnel flow (HHC).

3. Fe PROFILE MORPHOLOGY IN DR TAU

In this section, we quantitatively explore the kinematic structure of the Fe I and Fe II profiles in DR Tau and provide support for the interpretation that the permitted metallic lines in cTTS's arise in two physically distinct emission regions. In a future paper, we will extend this analysis to more lines in DR Tau and to a broader range of cTTS's.

The most obvious difference among Fe line profiles in any given spectrum of DR Tau is the range of line widths. Closer inspection reveals that there is a relation between the width of an Fe profile and the strength of that line. A similar effect has been previously reported for Fe lines in the cTTS RU Lup (Boesgaard 1984). This is illustrated in Figure 3, where four Fe I profiles from the $r_B = 8$ spectrum are displayed. It can be seen that as the equivalent width progresses from 0.03 to 0.9 Å, the FWHM increases from 26 to 67 km s^{-1}. Figure 4 shows that this behavior is characteristic of all the unblended Fe lines in our spectra. The figure plots the FWHM of an Fe line against its equivalent width and demonstrates that as the W_λ progresses from ∼0.05 to ∼0.5 Å, the FWHM increases by more than a factor of 3, from ∼20 to between 70 and 90 km s^{-1}, and remains roughly constant thereafter, up to the strongest line ($W_\lambda \sim 1$ Å in the red or ∼3 Å in the blue).

More subtle is the fact that the weaker Fe lines display a different profile morphology than the stronger lines. This is

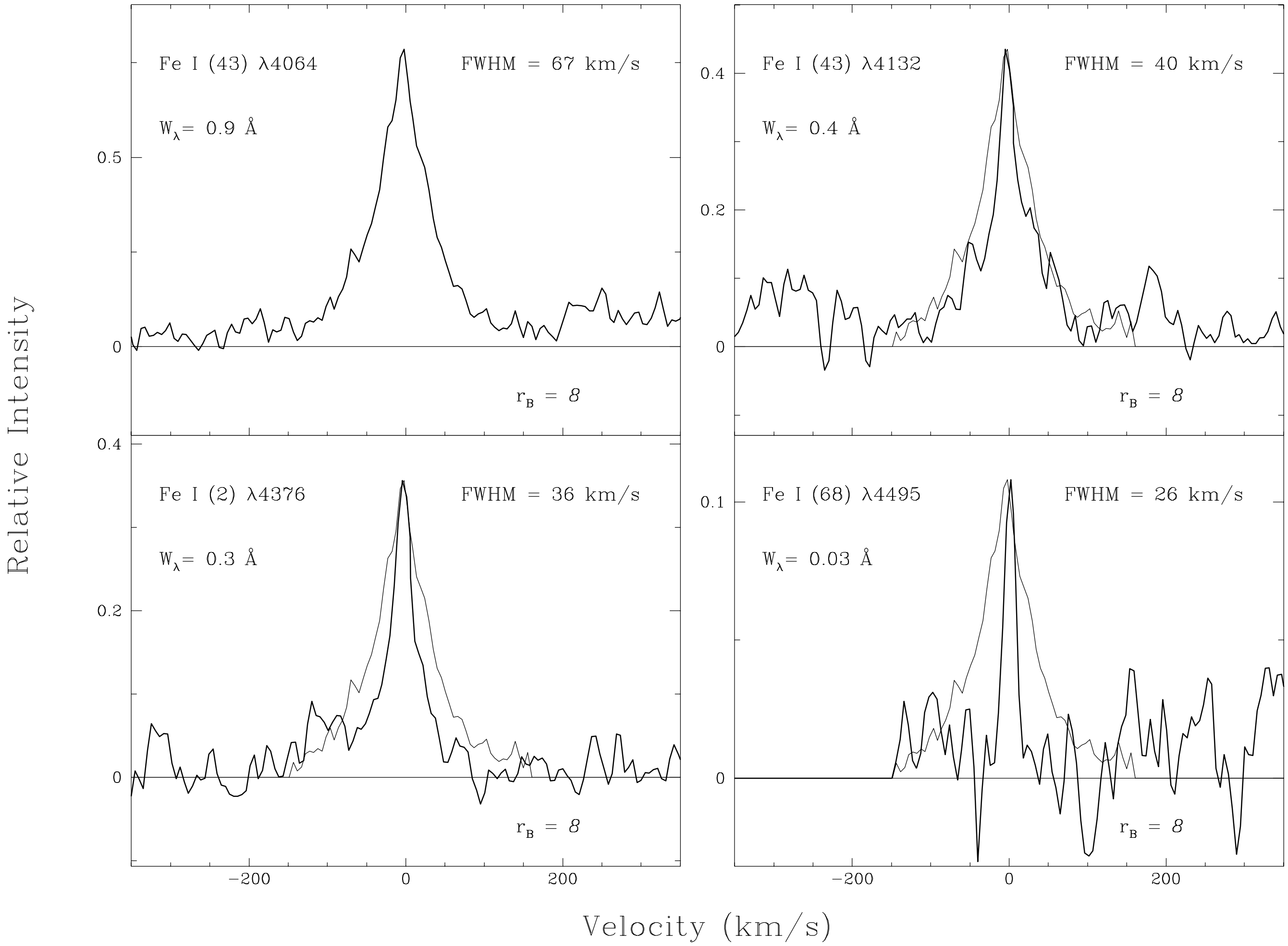

FIG. 3.—Four Fe I lines from the $r_B = 8$ spectrum show the variation in line width with line strength. The lines are ordered from the strongest to the weakest line, with the profile of the strongest line superposed on each profile. As the W_λ decreases from 0.9 to 0.03 Å, the FWHM decreases from 67 to 26 km s^{-1}.

clearly demonstrated by fitting each profile with a single function. The fitting procedure uses a χ^2 minimization to evaluate the best definition of the profile according to three fitting parameters: shape (β), width (δ), and velocity centroid (μ). The fitting function is

$$f(x) = e^{-\ln 2(|x-\mu|/\delta)^\beta} .$$

When functions of this form are fit to the unblended Fe profiles, we find that the shape parameter evolves from Gaussian (e^{-x^2}; $\beta = 2$) to exponential (e^{-x}; $\beta = 1$) as the line increases in W_λ from <0.1 Å up to several Å.

The large line widths of Fe likely arise from bulk kinematic motions. Then the dissimilarities in Fe line widths and profile shapes suggest that more than one kinematic regime may exist, with the emitting gas characterized by differing Fe I/Fe II abundance ratio and physical conditions. This possibility leads us to try the next simplest fitting procedure and to separate each line into two components to see if the variety of line profiles can be more succinctly described. Accordingly, we fit each line profile with two Gaussian components ($\beta = 2$) and iterate to find the component widths (δ_1 and δ_2) and velocity centroids (μ_1 and μ_2) that produce the best fit. In this case the fitting function has the form

$$f(x) = \alpha e^{-\ln 2(|x-\mu_1|/\delta_1)^2} + (1-\alpha)e^{-\ln 2(|x-\mu_2|/\delta_2)^2} ,$$

where α gives the relative peak amplitude of the two components.

A comparison of both fitting procedures, a single-component fit with a "free" shape parameter and a two-component fit with forced Gaussian shapes, is illustrated in Figure 5 for an Fe I line with a FWHM of 30 km s^{-1} and an W_λ of 0.3 Å, and an Fe II line with a FWHM of 59 km s^{-1} and an W_λ of 0.4 Å. Both lines are fit equally well by either a single function with an exponential form or by the sum of two Gaussian components. Note that the two Gaussian components naturally define a *narrow* and a *broad* component (NC and BC, respectively), but that the relative contribution of the two components differs between the Fe I and Fe II profiles. The relative amplitudes of the two components in each profile are given by α and 1-α, which we rename α_{NC} and α_{BC} for clarification. In this comparison, $\alpha_{NC} = 0.6$ for the Fe I line and $\alpha_{NC} = 0.35$ for the Fe II line.

While both approaches yield equally good fits for any individual line, what distinguishes the two-component Gaussian fitting procedure is that the derived parameters of each component (width and velocity centroid) are found to be highly consistent, not only for all the Fe lines in a given spectrum but also among all observing epochs. This uniform set of parameters for the NC and BC is illustrated in Figures 6 and 7. The widths of both the NC and BC are displayed as a function of line strength for all seven observ-

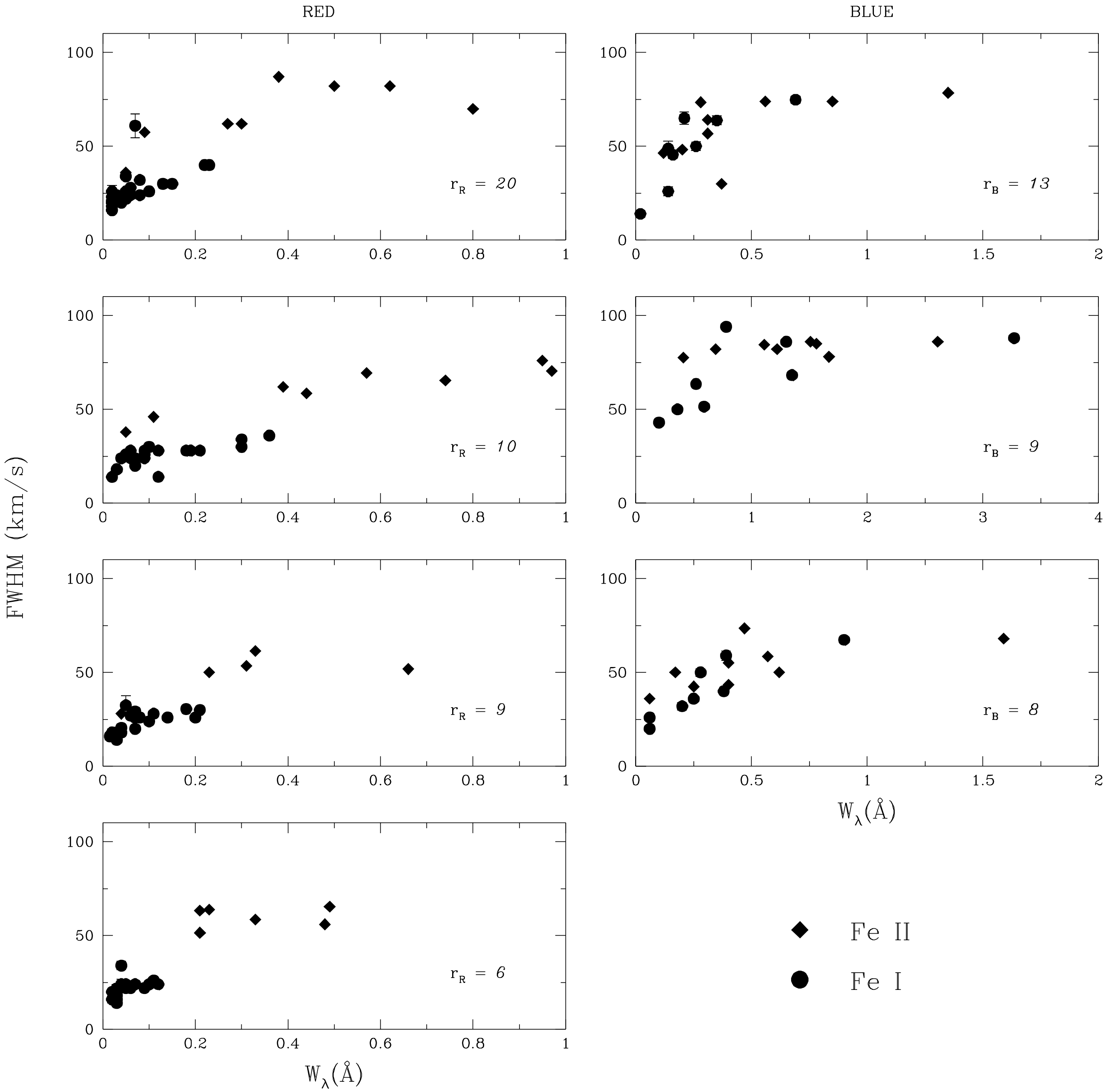

FIG. 4.—FWHM of the 62 unblended Fe I and Fe II profiles is plotted against the line W_λ for each epoch of observation, illustrating the trend of increasing line width with increasing line strength. The four red spectra are in the left-hand panels, the three blue spectra are in the right-hand panels, and both are ordered by veiling. Circles denote lines of Fe I and diamonds denote lines of Fe II.

ing epochs in Figure 6. Remarkably, the FWHM found for the NC averages 22 ± 4 km s^{-1} for all Fe profiles among six of the seven observing epochs. (The one exception, which will be discussed below, is from the spectrum $r_B = 9$.) The BC is not detectable in the weakest lines, which are best fitted by single-Gaussian profiles, but for $W_\lambda > 0.1$ Å, the BC is described by an FWHM that averages 102 ± 7 km s^{-1} in six of the seven observing epochs (the exception is the same spectrum, $r_B = 9$, discussed below).

The centroid velocities for each component, illustrated in Figure 7, also display a remarkable uniformity among all the lines and all but one observing epoch ($r_B = 9$). The NC is always centered on the photospheric velocity to within ± 5 km s^{-1}. Most of the time the BC is slightly blueshifted, by 5–10 km s^{-1}, and at any epoch the BC centroid velocity shifts are found to be similar among all Fe lines in the spectrum.

The exception to the uniform set of parameters derived for the NC and BC is from the blue spectrum with $r_B = 9$. This spectrum is unique in that the Fe lines are a factor of 2 stronger in W_λ than those from the other two blue epochs. While the formal χ^2 search for a two-component fit yields NC and BC widths a factor of 1.5 to 2 times greater than those for the six other observing epochs, we attribute this to a very small contribution from a 20 km s^{-1} wide NC at this epoch. Indeed, if we force the NC to a width of 20 km s^{-1}

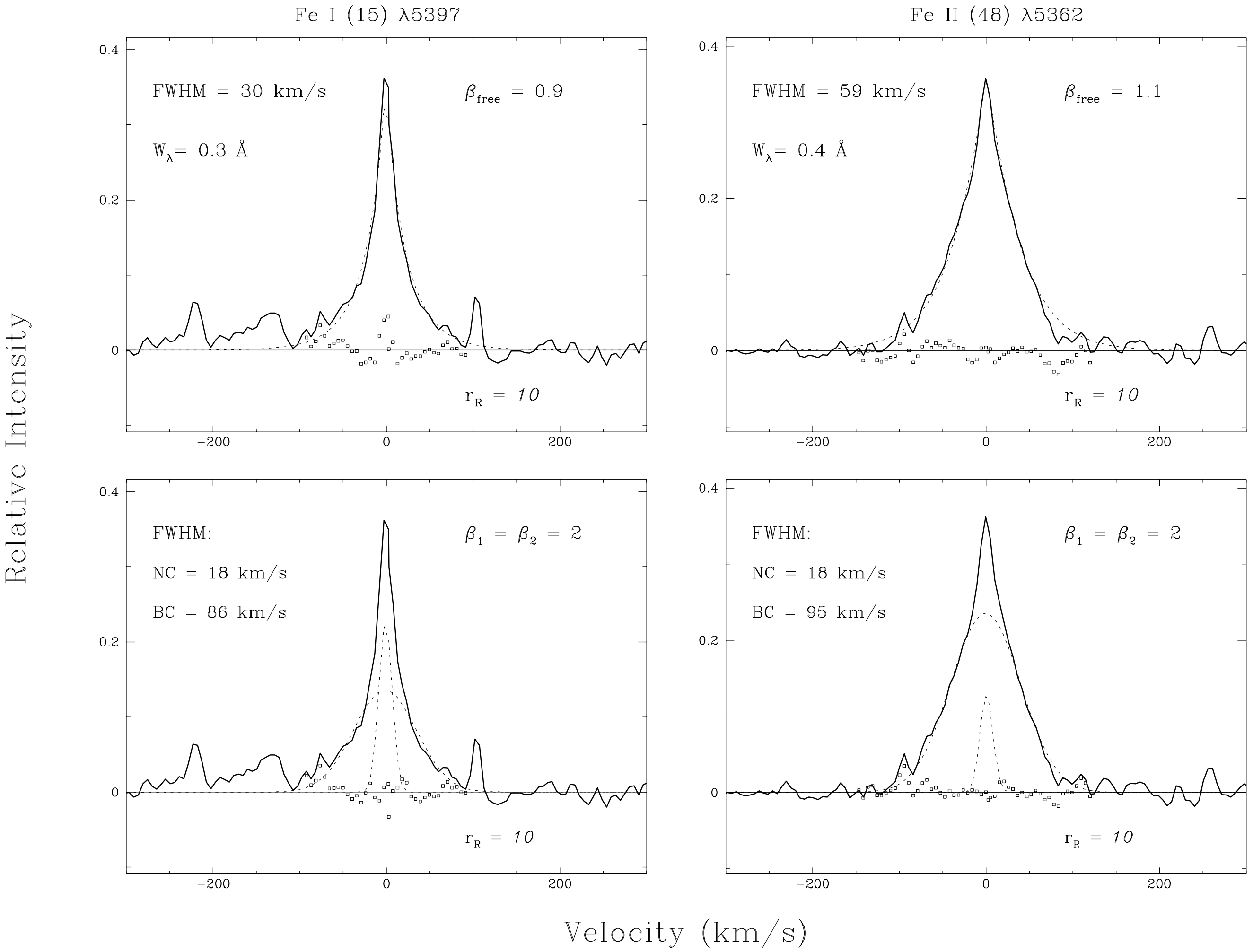

FIG. 5.—Comparison of the goodness of fit for the "single-free shape" and "double-Gaussian" functions is shown for a representative profile of Fe I (15) and Fe II (48) at the $r_R = 10$ epoch. The two upper panels show the single-function fits resulting from a χ^2 search for the best shape parameter, β. For both, $\beta \sim 1$, corresponding to an exponential form, although the Fe II line is twice as broad as Fe I. The bottom panels show the double-Gaussian fits for the same two profiles, with each profile decomposed into a narrow component (NC) and a broad component (BC), which are shown by dashed lines. The resultant line widths for the NC and the BC are nearly identical for the two ions. In each panel, the small open squares are the residuals between the observed and computed profiles.

and center it on the line peak, a search for the best parameters for the BC not only produces acceptable fits to the profiles but results in BC widths averaging 110 ± 10 km s^{-1} among all the Fe lines in this spectrum. Although no photospheric lines are detected in this heavily veiled spectrum, the resultant BC centroids lie within -4 ± 3 km s^{-1} of the NC centroids. These BC parameters are fully consistent with the parameters derived for the other observing epochs, and we attribute the failure of the χ^2 search to find the same parameters to the very small contribution from the NC at this epoch. This is illustrated in Figure 8, where both the free and the constrained NC fits for two representative lines from the $r_B = 9$ epoch are shown. It can be seen that the NC and BC parameters derived for the other six observing epochs are consistent with the data, but the weakness of a 20 km s^{-1} wide NC ($\alpha_{\rm NC} \sim 0.2$) for the $r_B = 9$ spectrum leads the χ^2 search to a different solution space. We thus adopt the interpretation that the parameters describing the NC and BC apply at all seven observing epochs.

The consistent set of profile parameters for the NC and BC emission supports the notion that there are two distinct regions of Fe emission in DR Tau. We have made no attempt to fit the occasional IPC redward absorption that is sometimes present in the strongest Fe II lines. Typically this feature is redward of the BC emission wings, and the consistency in the fit parameters found among the entire set of unblended Fe lines suggests that the two-component fit is a reasonable approximation to the Fe emission profiles.

In the next section, we use the different ratios of NC to BC emission found among unblended Fe lines to estimate the extent to which the physical conditions in these two regions differ. To obtain a consistent determination of the relative amplitudes and equivalent widths for the two components for this analysis, we have refit each line with the following restrictions: (1) the NC width is set at 20 km s^{-1}, and its velocity is at rest with respect to the line peak; and (2) the BC width is set at 100 km s^{-1}, and its centroid velocity is a free parameter. In all cases, the normalized peak amplitude of one of the two Gaussian components is also a free parameter ($\alpha_{\rm NC} + \alpha_{\rm BC} = 1$). In the remainder of the paper, the peak amplitudes and the equivalent widths of the two kinematic components will refer to those derived from these "forced" fits, rather than from the unconstrained fitting shown in Figures 6 and 7.

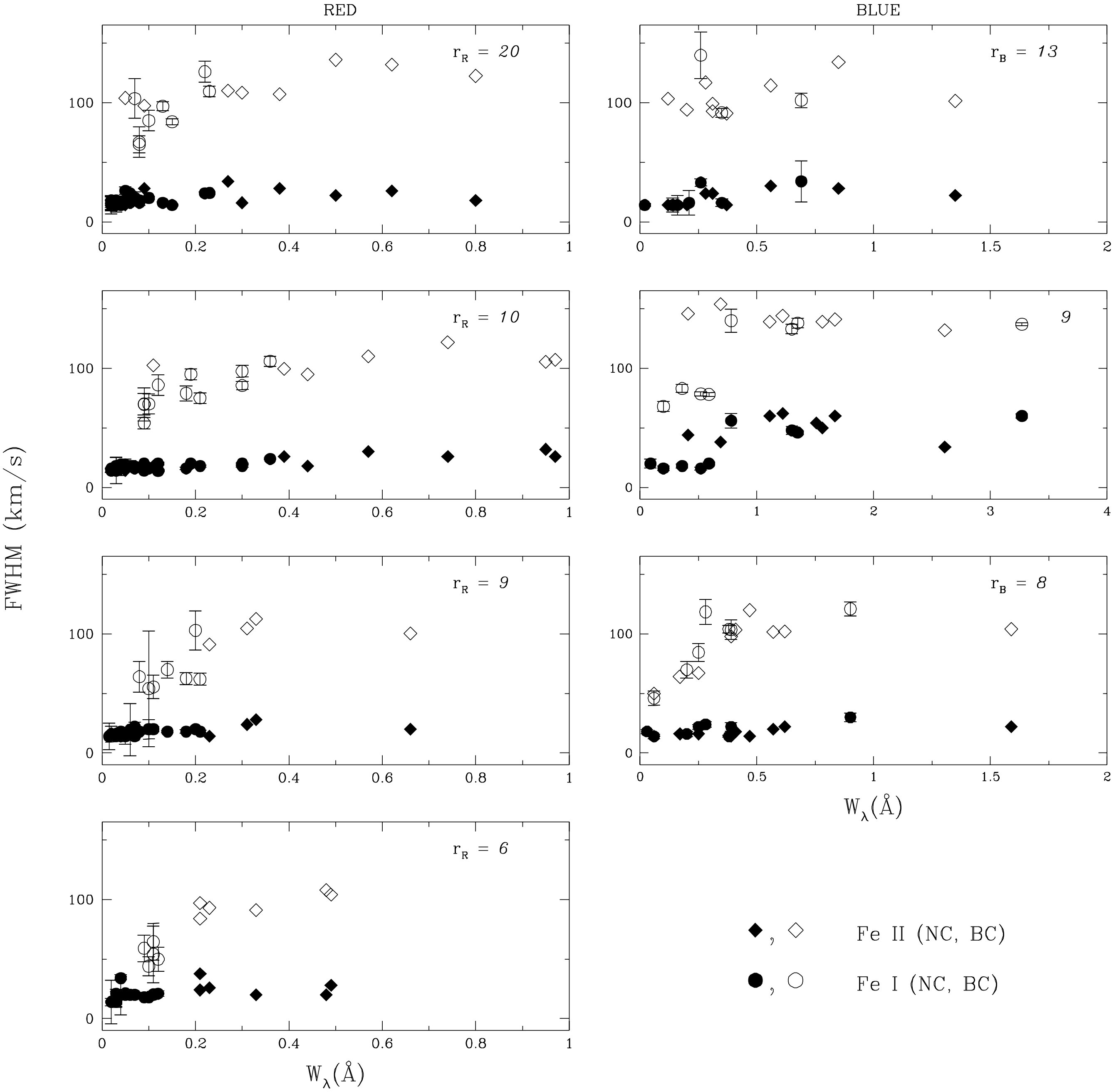

FIG. 6.—FWHM for each of the two Gaussian components that together fit the 62 unblended Fe I and Fe II profiles is plotted against the line equivalent width. Each panel is a different observing epoch, with Fe I lines plotted as circles, and Fe II lines as diamonds. The average FWHM of the NC (*filled symbols*) from all measurements except those from the $r_B = 9$ spectrum is 22 ± 4 km s^{-1}. The average FWHM of the BC (*open symbols*) from all lines with $W_\lambda >$ U0.1 Å, except for the $r_B = 9$ spectrum, is 102 ± 7 km s^{-1}.

The observed behavior of the Fe profiles, with a systematic relation between the strength of a line and its width and profile morphology, is thus accounted for by differing amplitudes of the NC and BC among lines of differing excitation and ionization. The nature of this relation is illustrated in Figure 9, where the two Gaussian component fits are shown for four Fe I lines from the $r_B = 8$ spectrum. There is a progression in the proportion of NC to BC emission, from the weakest line, dominated by the NC ($\alpha_{NC} = 1.0$), to the strongest and broadest line with the smallest proportion of NC to BC emission ($\alpha_{NC} = 0.3$). This trend is characteristic of all of our 62 unblended lines for all observing epochs, as shown in Figure 10, which plots the NC amplitude, α_{NC} (evaluated with the "forced" fits), as a function of line strength. The weakest lines have $\alpha_{NC} \sim 1.0$, and as line strength increases α_{NC} decreases, so that the strongest lines are typically characterized by $\alpha_{NC} \sim 0.3$, except in the $r_B = 9$ spectrum, where the strongest lines have $\alpha_{NC} \sim 0.1$.

We see no link between the Fe profile morphology and the continuum veiling. In our red spectra, the veiling varies by a factor of 3, but it is fairly constant in our blue spectra. The Fe profile morphology for any given line varies by $<40\%$ in the ratio of NC to BC equivalent widths, although the total emission equivalent widths for a given line vary by a factor of 2 or more in our spectra. The lack of any correlation between the Fe lines and the veiling is con-

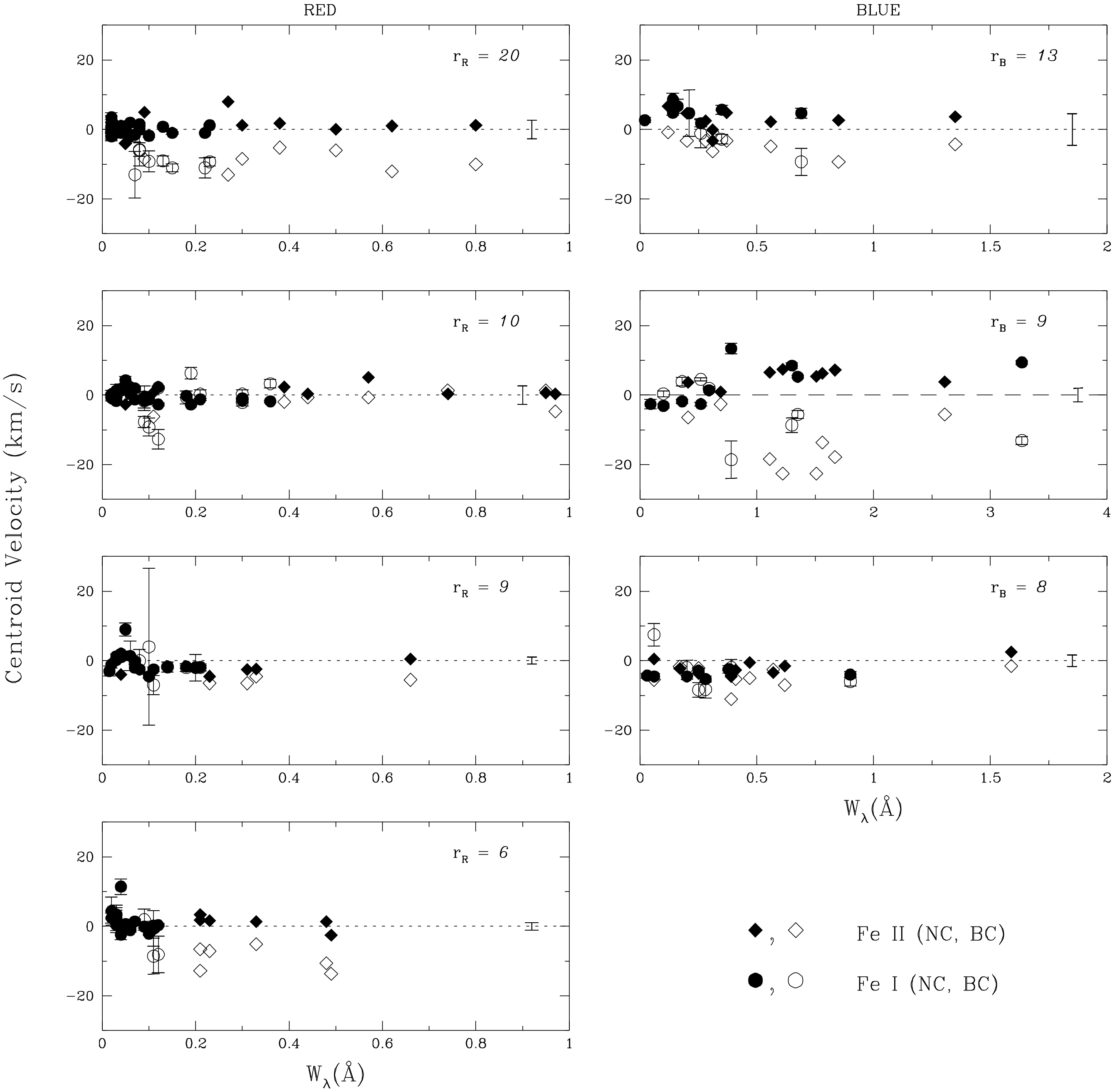

FIG. 7.—Velocity centroid of each of the two Gaussian components is plotted against the line equivalent width. Each panel is a different observing epoch, with Fe I lines plotted as circles, and Fe II lines as diamonds. Velocities are relative to the stellar photosphere, except for the $r_B = 9$ spectrum, whose photospheric lines are too weak, and the measurements are relative to the average peak velocity for each ion. The average velocity of the NC from all measurements except those from the $r_B = 9$ spectrum is -1 ± 2 km s^{-1}. The average velocity for the BC varies from one epoch to another, ranging from 0 to -11 km s^{-1}. Error bars about the line of 0 velocity indicate the uncertainties in the photospheric velocity.

sistent with the recent study of Hessman & Guenther (1997), who find that the line flux in cTTS's varies independently of the veiling.

4. DERIVATION OF PHYSICAL QUANTITIES FROM Fe LINES

For Fe, the availability of transitions originating from the same upper level provides an opportunity to compare the intensities of these lines without concern for how their common upper level is populated. This eliminates the need to perform excitation calculations and allows one to draw conclusions without the uncertainties inherent in adopting input parameters, such as collisional cross sections. In this section we use the intensity ratios of such lines to evaluate the optical depth, column density, and kinetic temperature in the Fe line formation region and to search for physical differences between the two kinematic components. We begin by comparing observed line ratios with their optically thin values, and we then employ the Sobolev large velocity gradient (LVG) approximation to interpret the observed differences between NC and BC emission. While the method described here is in principle an excellent diagnostic of the physical conditions in the Fe line formation region of DR Tau, restrictions of the current data set limit the extent to which we can draw firm conclusions.

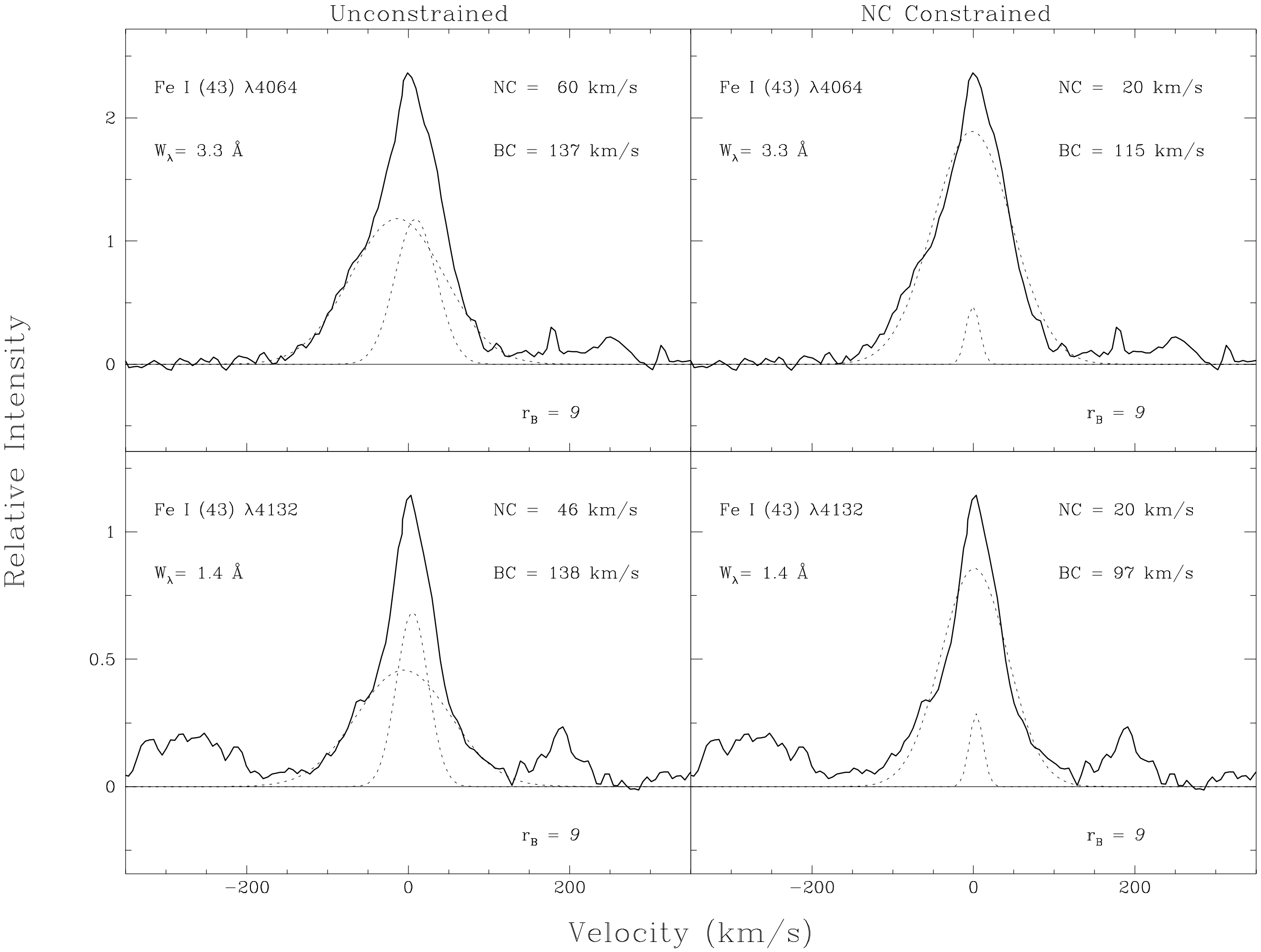

FIG. 8.—Left- and right-hand panels compare the unconstrained and constrained fits for the anomalous $r_B = 9$ spectrum. *Left-hand panels*: The two Gaussian components resulting from an unconstrained χ^2 search on two Fe I profiles yield NC and BC widths significantly broader than those at other epochs. *Right-hand panels*: The two Gaussian components resulting from a constrained χ^2 search, with the NC forced to have a width of 20 km s^{-1} and a velocity centroid at the line peak, are shown for the same two profiles. In each panel, the NC and BC fits to each profile are shown as dashed lines. The constrained fits yield NC and BC parameters that are consistent with those found from the χ^2 search at all other epochs. What distinguishes the $r_B = 9$ epoch is the very low peak amplitude of a 20 km s^{-1} wide NC, with $\alpha_{NC} = 0.2$.

4.1. *Relative Line Opacities From Line Pairs with Common Upper Levels*

The intensity ratio of two lines originating from the same upper level gives a direct measure of the line opacity. We will refer to each common upper level pair as comprising a weak and a strong member, labels that refer to the relative magnitude of their spontaneous emission or A_{ij} rates. By examining the intensity ratios from such line pairs, a comparison can be made of the relative optical depth of the two kinematic components.

An ideal pair to use for this type of analysis would be Fe I (41) λ4405 and Fe I (168) λ6394, with an A_{ij} ratio of 42 and $W_\lambda \sim 0.5$ and 0.05 Å, respectively. Unfortunately the members of this pair fall on two different grating settings with the KPNO echelle and thus were not observed simultaneously by us. Although the nonsimultaneity invalidates their use in our analysis, we show the profiles of each pair member in Figure 11 in order to illustrate how different the proportion of NC to BC emission can be between lines from a common upper level. The contrast between the profiles is dramatic, with the NC dominating the profile of the weaker transition [Fe I (168) λ6394; $\alpha_{NC} \sim 0.9$] and the BC dominating the profile of the stronger transition [Fe I (41) λ4405; $\alpha_{NC} \sim 0.2$]. This distinction can be further quantified by the ratio of NC/BC equivalent width for each line, which differs by approximately an order of magnitude between the weak and the strong line. This contrast is inherent in the Fe line formation region and cannot be attributed to time variability, as demonstrated by the near constancy of the profile morphology of each line over all observing epochs.

With the current data set, however, we must restrict our comparison of common upper level lines to pairs that are simultaneously observed in either our red or our blue spectral region. Despite the fact that we have 62 unblended Fe I and Fe II lines, the number of pairs meeting this criterion is limited to six. Five pairs are from Fe I, with three from Fe I (15) in the red, one from Fe I (168) in the red, and one from Fe I (43) in the blue. The fluorescent condition of the Fe I (43) multiplet does not affect this analysis, since the mode of exciting the upper level is not relevant. The single Fe II pair is in the blue, formed of lines from two multiplets, one from Fe II (27) and one from Fe II (38).

The proportion of NC to BC emission among these six pairs follows the pattern we have seen for the 62 unblended

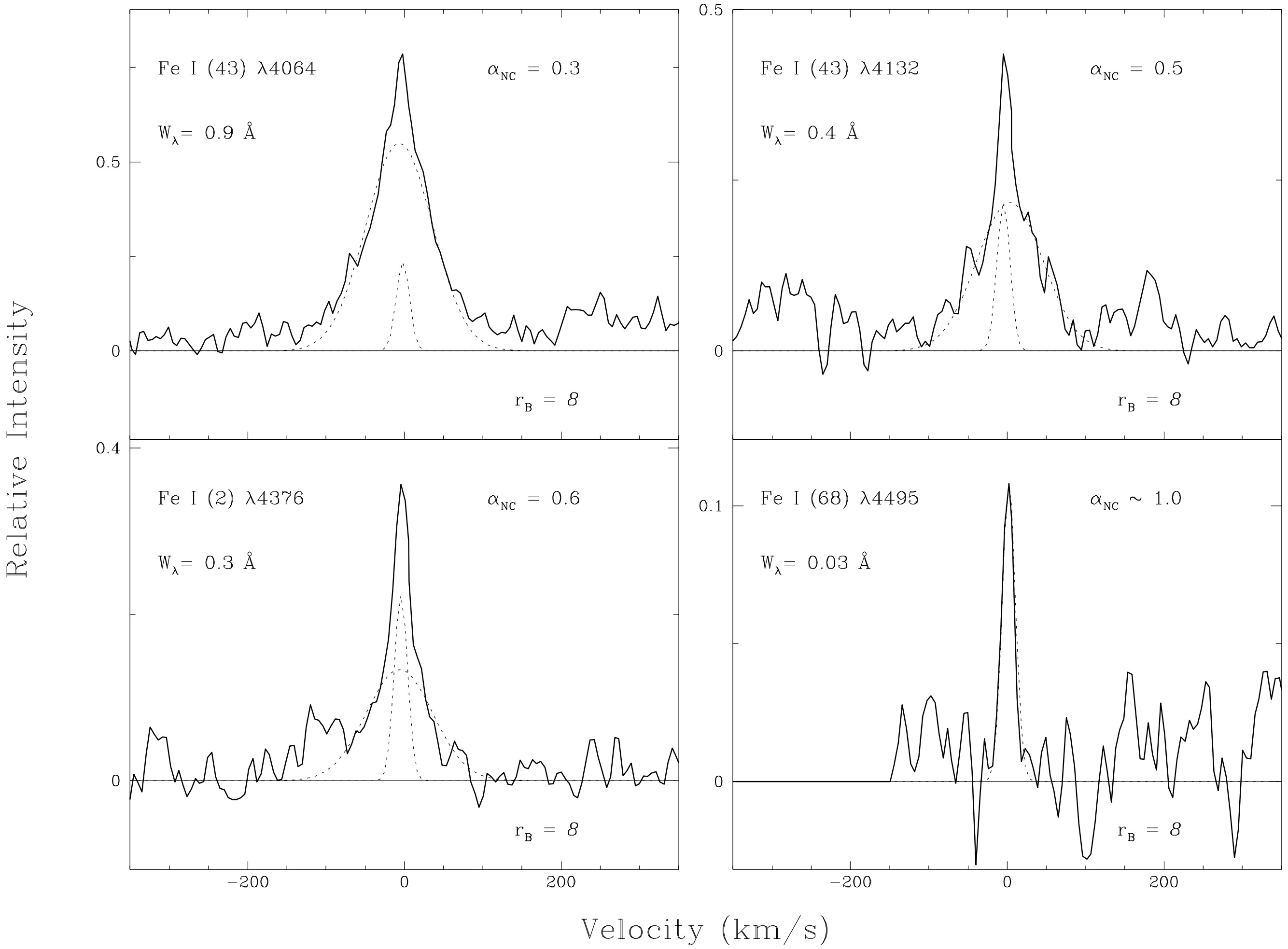

FIG. 9.—Four Fe I profiles from the $r_B = 8$ spectrum (identical to the set from Fig. 3) are selected to illustrate how the NC peak amplitude, α_{NC}, depends on line strength. For each profile, the two Gaussian components are shown with dashed lines. For the weakest line, $W_\lambda = 0.03$ Å and $\alpha_{NC} = 1.0$, while for the strongest line, $W_\lambda = 0.9$ Å and $\alpha_{NC} = 0.3$.

Fe lines and for the nonsimultaneous Fe I (41), Fe I (168) pair, with the BC emission becoming increasingly dominant in the stronger lines. The profiles for these six pairs are shown in Figures 12*a* and 12*b*, with pair members in adjacent panels.

Unfortunately, several factors impose limitations when using these six pairs for our analysis. (1) The ratios of the spontaneous transition rates only span factors of 7–17 among the six pairs, limiting their sensitivity as discriminants of physical conditions such as optical depth and column density. (2) As a result of the modest range of A_{ij} ratios, the contrast in the profile morphology between the weak and the strong line in a pair is less dramatic than that in the nonsimultaneous pair discussed above. (3) The small total W_λ of the weak line in each pair results in low S/Ns in the line wings and makes the extraction of the BC equivalent width somewhat uncertain. Hence, while the method we describe is in principle an excellent diagnostic, the limitations from this particular data set mean that our analysis should be considered illustrative rather than definitive.

We can quantify the comparison between the weak and strong lines in a pair by evaluating the NC/BC equivalent width ratio for both lines. This is illustrated in the upper panel of Figure 13 for the cases where both kinematic components could be reliably extracted for both the weak and strong line. In the figure, the ratios $W_\lambda(\mathrm{NC/BC})_{\mathrm{weak}}$ and $W_\lambda(\mathrm{NC/BC})_{\mathrm{strong}}$ are plotted as functions of A_{ij}, with members of a pair joined by a dashed line. A larger ratio of NC to BC emission for the weaker transition is seen in most pairs, although the maximum contrast is typically a factor of 2, rather than the 1 order of magnitude found for the nonsimultaneous blue/red Fe I pair with an A_{ij} ratio of 42.

Under optically thin conditions, the intensity ratio of the weak to the strong line in the pair should be proportional to the ratio of their respective A_{ij} values. In the absence of spectrophotometric data, we will substitute equivalent width ratios for intensity ratios. Although some pair members can be separated from each other by several hundred angstroms, adopting a 10^4 K blackbody to model the heavily veiled continuum of DR Tau incurs errors of $<5\%$ when using equivalent widths rather than flux ratios. In the lower panel of Figure 13, we compare the equivalent width ratios between pair members, taken separately for the NC and BC. It can be seen (1) that for most pairs the ratio of the weak to the strong line in both the NC and the BC exceeds the optically thin value, indicating that in both components at least the stronger line is optically thick; and (2) that in most cases, the ratios of the weak to the strong

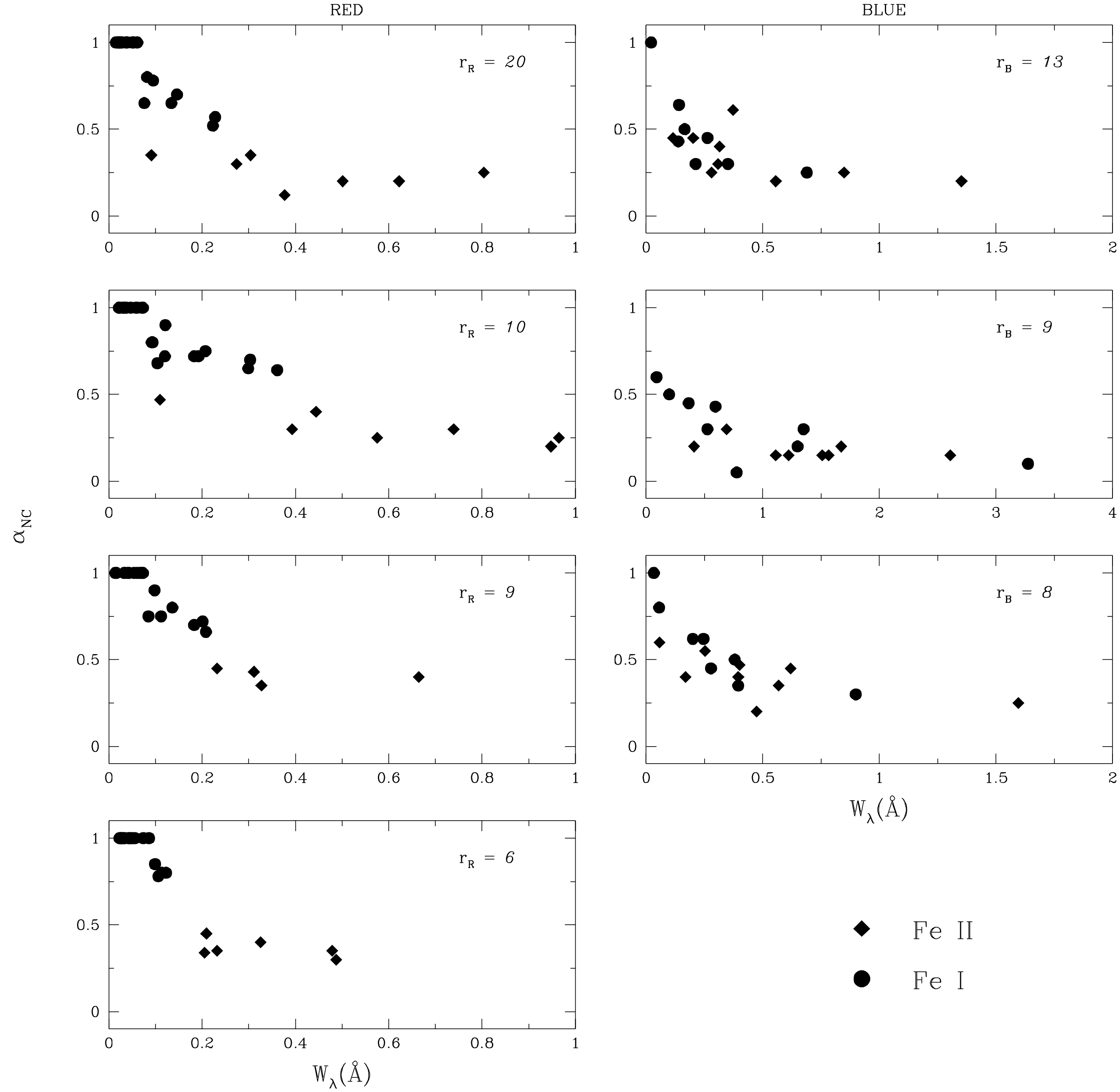

FIG. 10.—Relation between the NC peak amplitude, α_{NC}, and line strength for all 62 unblended Fe I and Fe II lines at each observing epoch is shown. The value of α_{NC} is ~1 for the weakest lines and is ~0.2 for the strongest lines. The exception is the $r_B = 9$ spectrum, where $\alpha_{NC} = 0.1$ for the strongest lines. In contrast to the fitting parameters shown in Figs. 6 and 7, here we show the α_{NC} that results when the constrained NC fitting procedure is applied to all lines (see text).

lines for the NC exceed those for the BC, suggesting a greater opacity in the NC lines.

4.2. *Line Opacities and Fe Column Densities from the Large Velocity Gradient Approximation*

To quantify the opacity and column density of the Fe line formation region, and to determine whether these differ for the NC and BC, we employ the Sobolev large velocity gradient (LVG) approximation to calculate the line opacity and local escape probability. Further, noting that the majority of our Fe I and Fe II lines have metastable lower levels, we can transform the line optical depths into column densities by assuming the metastable levels to be in thermal equilibrium with the ground state and neglecting the population in the nonmetastable levels.

The LVG approximation is probably appropriate for describing the BC emission, with a FWHM of ~100 km s^{-1}. However, for the NC emission, with a FWHM ~ 20 km s^{-1}, the LVG approximation may be less applicable. In this case it is likely to give a lower bound to the opacity, since the scaling of the local escape probability with line opacity is similar in the LVG and the static case, but in the static case the intensity ratio of two lines is not a simple ratio of their local escape probabilities.

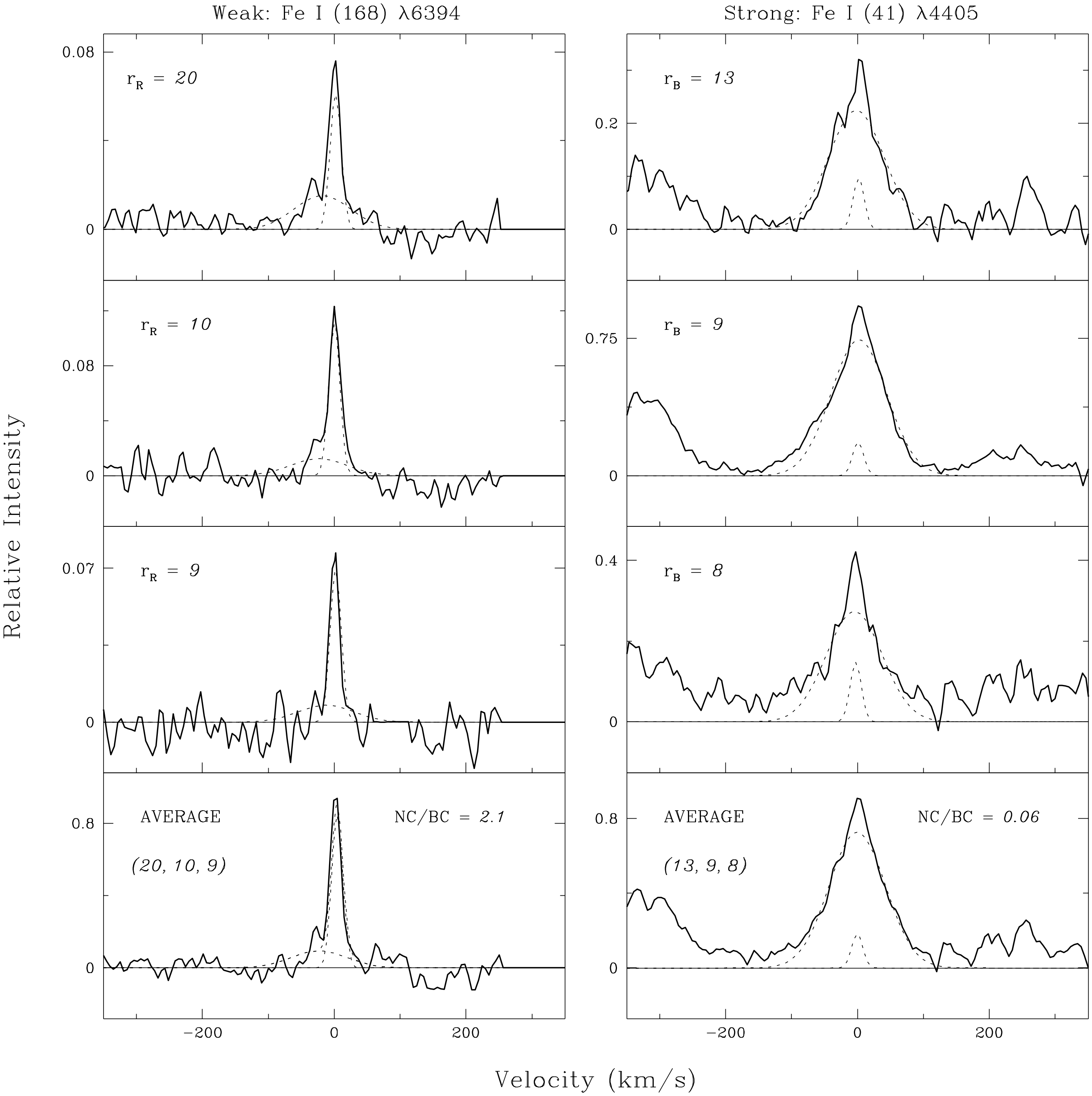

FIG. 11.—Pair of nonsimultaneous Fe I lines arising from a common upper level with an A_{ij} ratio of 42. The left-hand panels show three individual profiles of the weaker line in the pair, Fe I (168) λ6394, and the average of those three observations. It is seen that at all epochs this line is dominated by the NC, with $\alpha_{\rm NC} \sim 0.9$ and an equivalent width ratio of NC/BC = 2.1. In contrast, the right-hand panels show the individual and average profiles for the stronger line in the pair, Fe I (41) λ4405. In this line the BC contribution dominates at all epochs, with average values of $\alpha_{\rm NC} \sim 0.2$ and NC/BC = 0.06. In each panel, the NC and BC fits to each profile are shown as dashed lines.

In the Sobolev approximation, the intensity ratio of two transitions arising from the same upper level is given by

$$f_{ws} = \frac{\nu_w A_w \beta_w}{\nu_s A_s \beta_s}\,, \tag{1}$$

where A is the spontaneous emission rate, β is the escape probability, ν is the transition frequency, and the subscripts w and s subscripts refer to the weaker and stronger transition in each pair.

If the velocity gradient is isotropic, the escape probability averaged over all directions has the form

$$\beta = \frac{1\text{–}e^{-\tau}}{\tau}\,, \tag{2}$$

and the line opacity in the Sobolev approximation is

$$\tau = \frac{hc}{4\pi}\,\frac{(n_l B_{lu} - n_u B_{ul})}{dv/dl}\,, \tag{3}$$

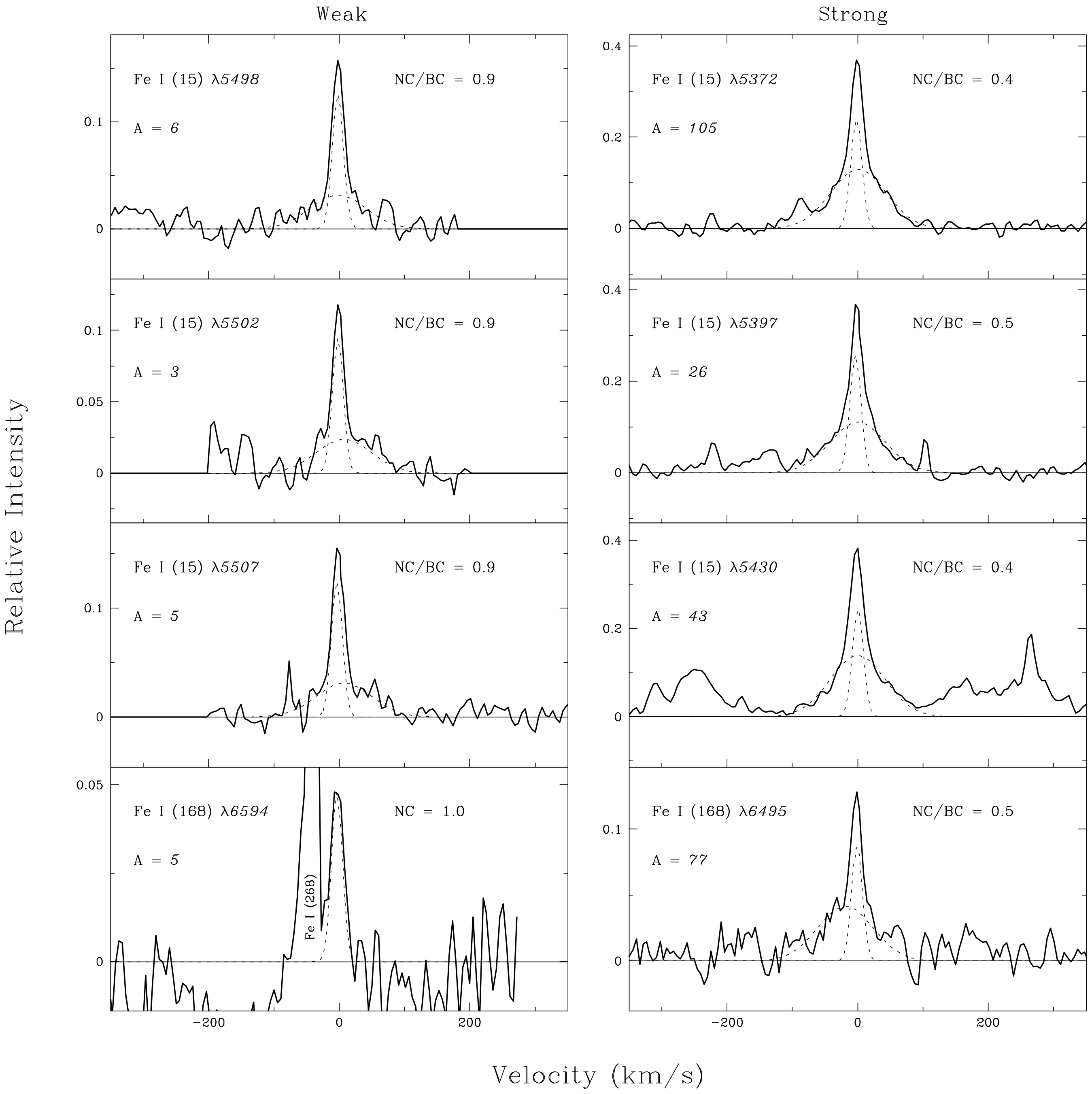

FIG. 12*a*

FIG. 12.—Profiles are shown for the six pairs of simultaneously observed Fe lines that arise from common upper levels. Each pair is composed of a weak (*left-hand panel*) and a strong (*right-hand panel*) member, where the labels refer to the relative strengths of their spontaneous emission rates A_{ij}, identified for each profile in units of 10^4 s^{-1}. (*a*) Four Fe I pairs from the $r_R = 10$ spectrum; (*b*) one Fe I pair and one Fe II pair from the $r_B = 13$ spectrum. In contrast to the nonsimultaneous pair in Fig. 11, the ratio of NC/BC emission for each member of a pair differs by only a factor of 2. In each panel, the NC and BC fits to each profile are shown as dashed lines.

where n_u, n_l are the upper and lower level population, B_{lu} and B_{ul} are the Einstein stimulated absorption and emission coefficients, and dv/dl is the velocity gradient. Neglecting the upper level population with respect to the population in the lower metastable level, and assuming a thermal distribution in the metastable levels, we obtain

$$\tau \approx \frac{hc}{4\pi} B_{lu} g_l \frac{e^{-E_l/kT}}{U(T)} \frac{n\,dl}{dv}\,, \qquad (4)$$

where $U(T)$ is the partition function from the metastable levels, n is the total ion number density, and E_l is the lower level excitation energy.

The intensity ratio f_{ws} is then a function of two unknowns, the velocity modified column density, $\mathcal{N} = n\, dl/dv$ and the kinetic temperature T. The left-hand panels of Figures 14*a* and 14*b* plot the predicted f_{ws} ratios as functions of $\mathcal{N}$ for T between 4000–20,000 K for each of our six common upper level pairs. Comparison of the observed f_{ws}

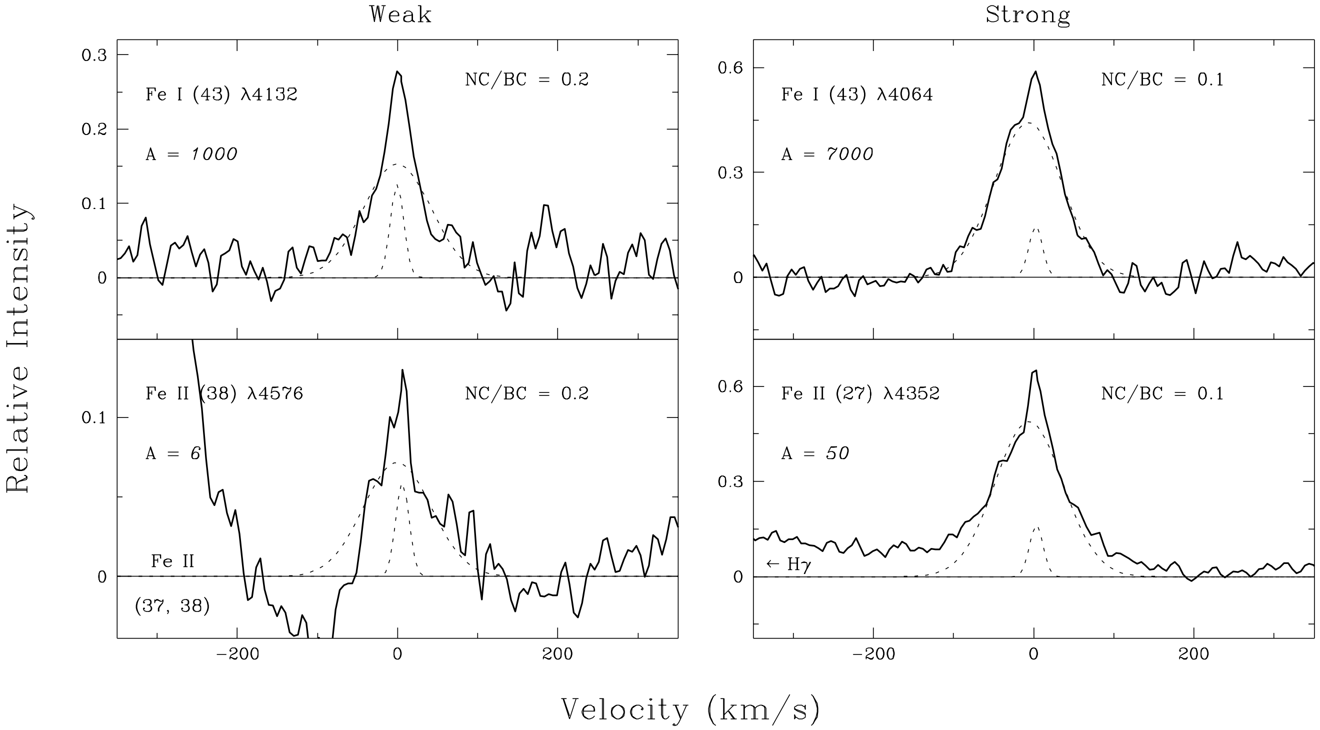

FIG. 12*b*

intensity ratio, measured separately for the BC and NC, with the predicted relations then yields a locus of $\mathcal{N}$ and T values that are compatible with the observations.

The theoretical dependence of the flux ratio on $\mathcal{N}$ at a fixed T is governed by the dependence of the escape probability on line opacity (see eqs. [1] and [2]). In the optically thin limit, the escape probabilities for both the weak and strong lines will be unity and f_{ws} will be a constant independent of $\mathcal{N}$ or T. As $\mathcal{N}$ increases, the strong line becomes optically thick first, causing f_{ws} to increase. As long as the weak line remains optically thin, f_{ws} will increase as the opacity in the strong line increases, creating the steeply rising part of the curve. Eventually $\mathcal{N}$ increases to the point where the weak line becomes optically thick and f_{ws} again becomes independent of $\mathcal{N}$. The shape of these curves of growth depends only on the line opacities, the effect of temperature being merely to displace the curves along $\mathcal{N}$. As shown in the left-hand panels of Figure 14, the observed f_{ws} typically falls on the near-linear regime of the curve where the stronger line of each pair is optically thick and the weaker line is optically thin. The observed f_{ws} can thus be translated into an opacity independent of the actual values of $\mathcal{N}$ and T.

In Figure 15 we plot the optical depths derived by this method for each kinematic component against the A_{ij} values. It can be seen that the opacities range from about 0.1 to 10 among the lines observed. However, as explained below, we have reason to doubt the applicability of these values to the blue Fe I (43) multiplet, which may have opacities considerably higher than indicated. The figure also suggests that the optical depth of the NC exceeds that of the BC by a factor of 2-4 in each line, consistent with the trend inferred from the comparison of the observed line ratios with their optically thin values shown in Figure 13.

Estimating the column density, which is more sensitive to temperature, proceeds as follows. An observed f_{ws} dictates a

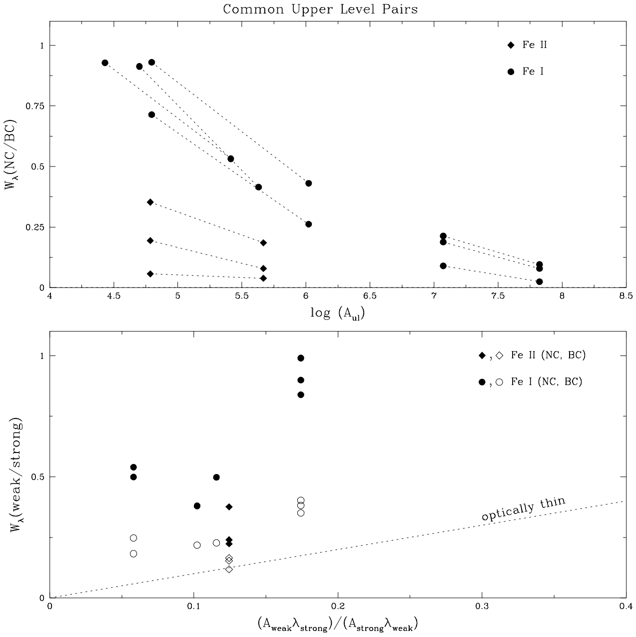

FIG. 13.—Comparison of the BC and NC emission between weak and strong lines in a common upper level pair, for those pairs where both components can be reliably extracted. From the four red epochs, this includes three pair of Fe I (15) lines from $r_R = 10$ and one pair of Fe I (15) lines from $r_R = 20$. From the three blue epochs, NC and BC could be extracted from all observations of the Fe I (43) and Fe II (38) line pairs. In the upper panel, the W_λ(NC/BC) ratio for each line is plotted against the spontaneous emission rate A_{ij}, with each member of a pair joined by a dashed line. In the lower panel, the W_λ(weak/strong) ratio, evaluated separately for the NC and the BC, is plotted against the expected flux ratio between pair members in the optically thin limit. For most pairs, the ratio of the weak to the strong line in both the NC and the BC exceeds the optically thin value, indicating that in both components at least the stronger line is optically thick. Also for most pairs, the ratio of the weak to the strong line for the NC exceeds that for the BC, suggesting a greater opacity in the NC line.

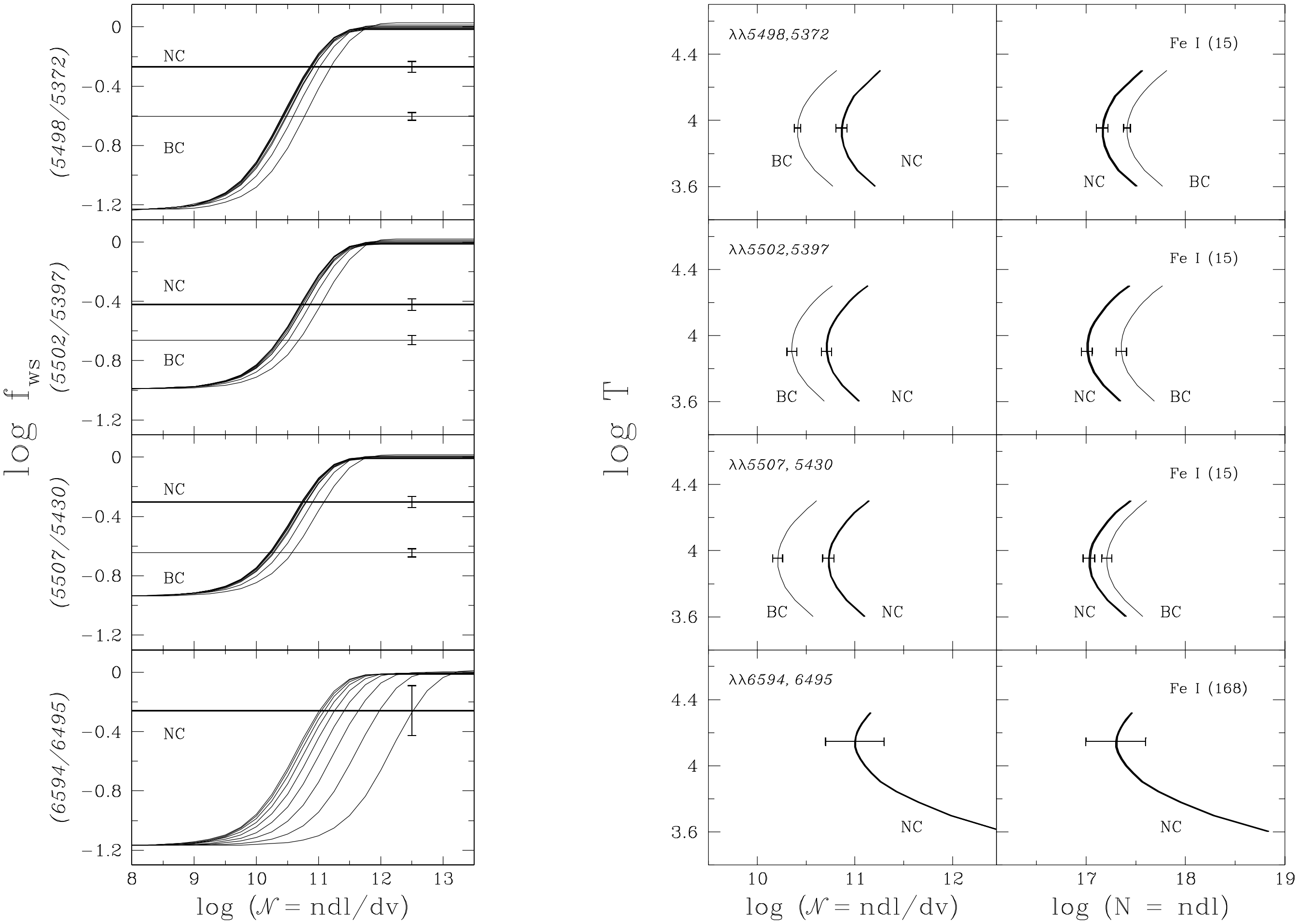

FIG. 14*a*

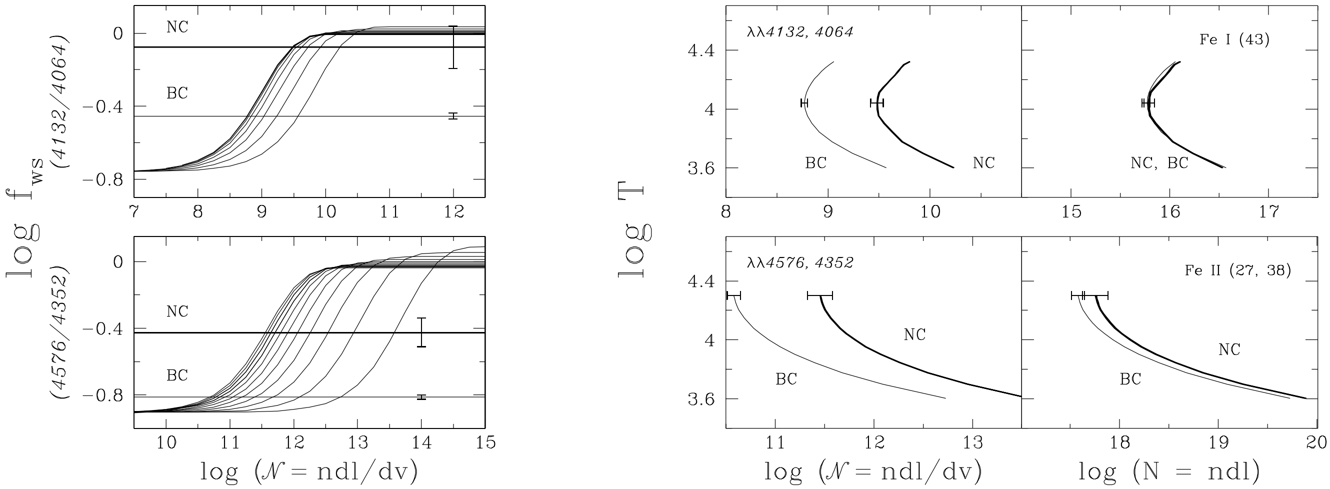

FIG. 14*b*

FIG. 14.—(*a*) Results from the Sobolev LVG calculations are shown in this sequence of plots for the four common upper level line pairs from our red spectra. *Left-hand panels*: Curves of growth relating f_{ws}, the intensity ratio of the weak to the strong line between members in each pair, to the velocity-modified column density, $\mathcal{N} = n\,dl/dv$. Growth curves in each panel are plotted for temperatures in the range from $4000 \leq T \leq 20{,}000$ K. Horizontal lines denote the observed values of f_{ws}, evaluated separately for the NC and the BC. *Center panels:* The theoretical loci of $\mathcal{N}$ and T that are compatible with the observed f_{ws} ratios shown in the growth curves. Separate loci are plotted for the NC and the BC ratios. *Right-hand panels:* The theoretical loci of N and T, where $N = n\,dl \approx \mathcal{N}\Delta v$, which are compatible with the observed f_{ws} ratios shown in the growth curves. In the conversion from the velocity modified column density to a standard column density, the application of the differing Δv for the two components shifts what were distinctly lower values of $\mathcal{N}$ for the BC to values of N that are essentially comparable between the two components. Thus for the temperature regime between 4000 and 20,000 K, we find no significant difference in the column densities of the two kinematic components. (*b*) Same as (*a*) but for the two common upper level line pairs from our blue spectra.

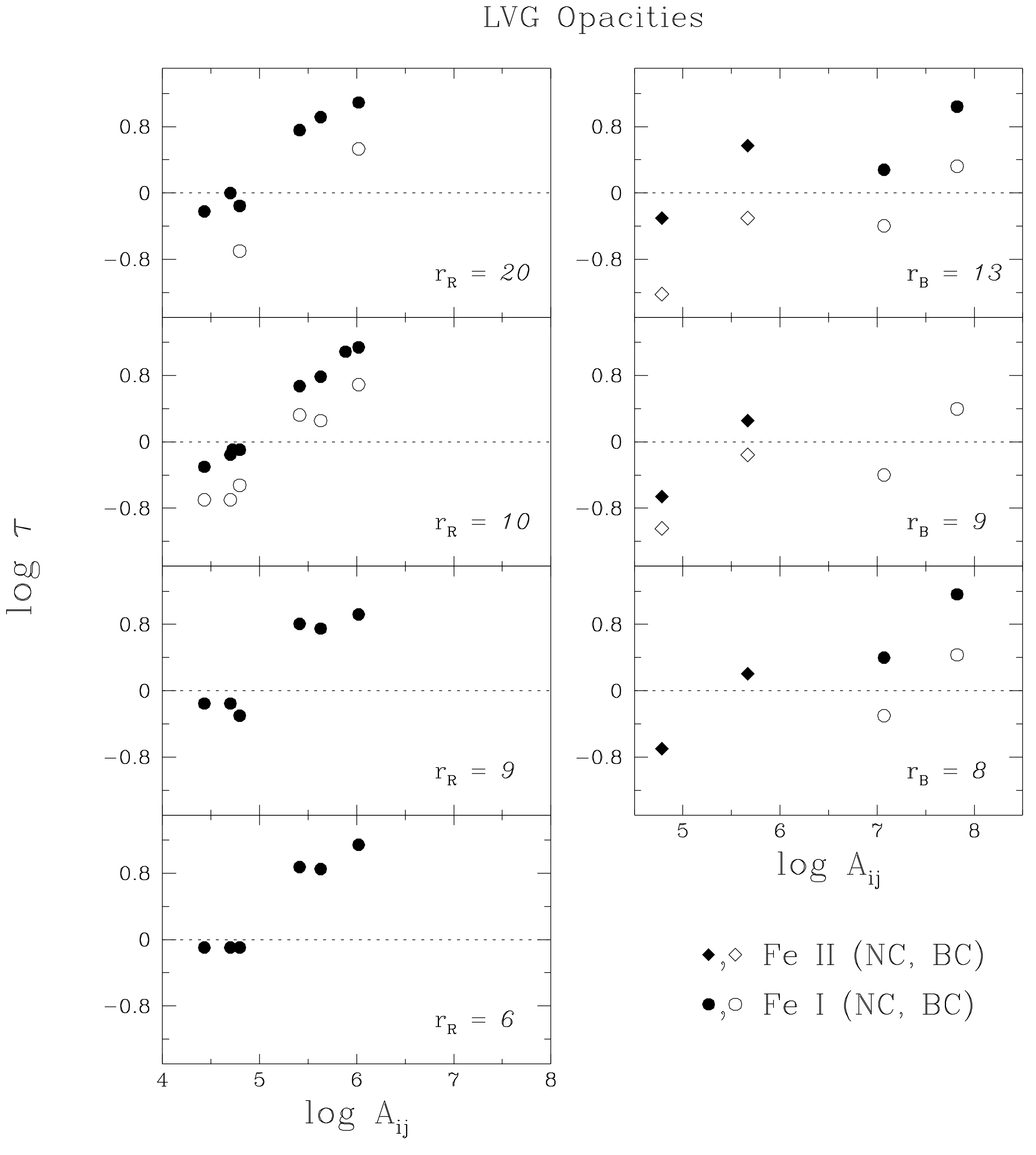

FIG. 15.—Opacities for the lines in our six common upper level line pairs, shown for each epoch of observation. The opacities can be derived from the growth curves of Fig. 14 but are independent of $\mathscr{N}$ and T (see text). Derived values range from about 0.1 to 10 for these lines. The data suggest that the optical depth of the NC exceeds that of the BC by a factor of 2–4 in each line, consistent with the trend inferred from the comparison of the observed line ratios with their optically thin values shown in Fig. 13.

theoretical locus of $\mathscr{N}$ and T values, as shown in the middle panels of Figure 14. In the allowed loci, $\mathscr{N}$ initially decreases, then increases, with increasing kinetic temperature, so that a given $\mathscr{N}$ corresponds to two possible values of T. This behavior occurs because a given f_{ws} on the rising portion of the curve of growth fixes the opacity in the strong line, as explained earlier, so that equation (4) simplifies to $\mathscr{N} \propto U(T)/e^{-E_l/kT}$. While the partition function $U(T)$ increases with T, the factor $1/e^{-E_l/kT}$ decreases with T and dominates at low temperatures. Therefore, as T initially increases from 4000 K, $\mathscr{N}$ decreases until T is high enough (at a value dependent on E_l) that $U(T)$ dominates the temperature dependence, after which $\mathscr{N}$ increases with increasing T.

The $\mathcal{N}$-T locus that accounts for the observed f_{ws} ratio can be converted to a column density-temperature relation through $N = n\,dl \approx \mathcal{N}\Delta v$. We adopt $\Delta v = 100$ km s^{-1} for the BC and $\Delta v = 20$ km s^{-1} for the NC and display the N-T loci corresponding to our observed intensity ratios in the right-hand panels of Figure 14. In the conversion from the velocity-modified column density to a standard column density, the application of the differing Δv for the two components shifts what were distinctly lower values of $\mathcal{N}$ for the BC to values of N that are essentially comparable between the two components. Thus for the temperature regime between 4000 and 20,000 K, we find no significant difference in the column densities of the two kinematic components, with the caveat that the small linewidth of the NC probably compromises the LVG approximation, so the N we derive provides only a lower bound on the column density of the NC region.

The magnitude of the derived column density depends on the kinetic temperature. However, at all temperatures, we consistently find that the column densities for Fe II are at least an order of magnitude larger than those for Fe I, indicating that Fe II is the dominant ionization state. A discrepancy exists, however, in the Fe I column densities derived from two different multiplets. Specifically, the column densities from the red Fe I (15) multiplet are consistently an order of magnitude greater than those derived from the blue Fe I (43) multiplet. For example, at temperatures $\sim$8000–10,000 K, the corresponding $N_{\mathrm{Fe\,II}} \sim 10^{18}$ cm^{-2}, while $N_{\mathrm{Fe\,I\,(15)}} \sim 10^{17}$ cm^{-2} and $N_{\mathrm{Fe\,I\,(43)}} \sim 10^{16}$ cm^{-2}. This discrepancy between the two Fe I column densities is far too large to be accounted for by observational uncertainty in the Fe I line ratios. It cannot be attributed to the nonsimultaneity of the blue and red spectra, since the discrepancy persists over the four red and three blue epochs and similar profile morphology is displayed by these lines at each epoch.

It is more likely that the discrepancy in the Fe I column densities results from a breakdown of the simplifying assumption of isotropy in the velocity gradient. In that case, the radiative transfer near the surface of the emission region and along certain directions within the emission region may resemble more the static than the LVG situation. The result is that photons in a line can originate from a range of optical depths, making our characterization of the emission by a single τ erroneous. This error is more severe for the more optically thick line. For this reason, we discount the result on $\mathcal{N}$ or N derived from the Fe I (43) lines, which, with A_{ij} values 70–2000 times larger than those in Fe I (15), have much larger opacities at the same column density. For example, if we adopt the Fe I opacity and column density derived from the Fe I (15) line pairs, then the corresponding optical depth for the fluoresced Fe I (43) lines would be several hundred. It also means that τ and $N_{\mathrm{Fe\,I}}$ determined from the Fe I (15) lines are only lower bounds. The $N_{\mathrm{Fe\,II}}$ we find is also a lower bound, although for the BC it provides the most reliable estimate since the optical depths found are so low, $\lesssim 0.7$.

In summary, application of the LVG approximation to the six pairs of available Fe I and Fe II lines indicates that Fe II is the dominant ionization state of iron. There is a suggestion that the NC is more optically thick than the BC in a given line. The current data set gives sufficiently large errors in the Fe column densities that distinctions between the NC and BC cannot be discerned. The most solid result of the LVG analysis to this restricted set of common upper level pairs is the estimate for the Fe II column density in the BC, with $N_{\mathrm{Fe\,II}} \sim 10^{18}$–$10^{19}$ cm^{-2} for kinetic temperatures in the range from 4000 K to 10,000 K. If one then assumes that most of the Fe is once ionized, this yields an approximate total column density for the BC region of $N_{\mathrm{H}} \sim 3 \times 10^{22}$–$3 \times 10^{23}$ cm^{-2}.

4.3. *Kinetic Temperature*

In principle, an estimate of the kinetic temperature in the Fe line formation region can be made by continuing the procedure from the previous section, where the comparison of intensities between a pair of lines from a common upper level defines an allowed $\mathcal{N}$-T or N-T locus. By superposing the loci from several line pairs, a simultaneous solution of temperature and column density will follow from their points of intersection. The success of this approach depends on maximizing the difference in excitation energy between line pairs. With our limited data set, the best lines we have are a pair of Fe I (15) lines with $E_{\mathrm{upper}} \sim 3.3$ eV and a pair of Fe I (168) lines with $E_{\mathrm{upper}} \sim 4.3$ eV. Unfortunately, the small W_λ in the Fe I (168) pair lead to uncertainties in the $\mathcal{N}$-T locus that are too large to identify a good estimate of the kinetic temperature by this method.

Making use of the fact that the excitation temperature of a collisionally excited line is not higher than the kinetic temperature, a lower bound on T can be roughly estimated. This follows from determining the luminosity of a very optically thick line, assuming an area for the emission region, and calculating the line excitation temperature that would reproduce that luminosity. We restrict ourselves to the luminosity of the narrow component for this exercise, since this component appears to be optically thicker in any given line. Furthermore, we have a better handle on the emitting area of the NC (see discussion in § 5), which we assume is between 0.05 and 0.2 of the stellar surface area. In our spectra, the strongest NC transition is Fe II (42) λ4924, and we estimate its luminosity as being 1.2×10^{30} ergs s^{-1}, based on our measured equivalent width, the average photometric state of DR Tau from Kenyon et al. (1994), $A_V = 3.2$ (HEG), and a distance to Taurus of 140 pc. For an NC emission area between $0.05A_*$ and $0.2A_*$, the corresponding lower bound on temperature ranges between $\sim$13,500 and $\sim$8400 K.

A third approach provides information on the *relative* kinetic temperature between the NC and BC regions. It relies on identifying transitions arising from widely different energy levels whose intensities are not sensitive to opacity. We have identified two such lines, described below, but again, in the current data set, this pair is observed nonsimultaneously. However, since this approach requires only the NC/BC flux ratio for each line, it will be valid as long as the profile morphology is not time variable. The opacity-insensitive transitions we have identified for this analysis are Fe I (2) λ4376 and Fe I (686) λ5616, arising from upper levels at 2.83 eV and 5.54 eV, respectively.

The insensitivity to opacity for the Fe I (2) λ4376 line comes from its being the dominant decay channel from its upper level and the estimate that its optical depth is not large. Specifically, its opacity depends on $\mathcal{N}$ and T roughly as $\tau \sim (\mathcal{N}/5.4 \times 10^{10}$ cm^{-3} s$)(10^4$ K$/T)$, and with $\mathcal{N} \sim 10^{11}$ cm^{-3} s for both the NC and BC (see Fig. 14*a*), τ is not more than a few. Since its spontaneous emission rate of $\sim 3 \times 10^4$ s^{-1} exceeds those of other decay routes from the same upper level by a factor of ≥ 50, emission of λ4376 will be the dominant radiative decay process when this level is populated. The additional assumption that collisional deexcitation is not important, in light of λ4376's large A_{ij} rate and modest optical depth, results in a probability near unity that a λ4376 photon will be emitted following every excitation of the upper level, independent of the opacity.

The insensitivity to opacity for the Fe I (686) λ5616 line, which is the strongest transition from its upper state, comes from the fact that it maintains its optically thin branching fraction independent of the optical depth. The λ5616 line has a large A_{ij} rate of $\sim 2.6 \times 10^7$ s^{-1} and a branching fraction of ∼42% in the optically thin limit. The next two most important decay channels from the same upper state are Fe I (553) λ5324 and Fe I (816) λ6400, with A_{ij} rates of 2.1×10^7 s^{-1} and 9.3×10^6 s^{-1}, and branching fractions of 32% and 14.6%, respectively. All of these transitions have nonmetastable lower levels at comparable energies, ∼3.4, 3.3, and 3.6 eV, respectively, which possess large and comparable decay rates ($A_{ij} \sim 1 \times 10^7$ s^{-1}). As $\mathcal{N}$ grows, the opacities of λ5616, λ5324, and λ6400 will be similar and increase slowly and in tandem because of the nonmetastable nature of their lower levels. This results in their branching fractions remaining nearly uniform at their optically thin values. Fairly independent of its opacity then, Fe I λ5616 will account for ∼42% of the radiative decays from its upper level *in both the NC and the BC*.

For both of these opacity insensitive lines, if collisional excitation is assumed, the line intensity will be determined by the kinetic temperature and the product of the collisional cross section times the electron density times the Fe I number density times the emitting volume. If the collisional rate constants of the upper states of λ5616 and λ4376 were known, then $T_{\rm NC}$ ($T_{\rm BC}$) could be obtained directly from the NC (BC) flux ratio between the two lines, provided that simultaneous flux ratios were available. Without knowledge of the collisional rate constants, we can take the NC/BC flux ratio for each profile to eliminate the dependence on collisional cross section. Then the relative values of $T_{\rm NC}$ and $T_{\rm BC}$ can be compared by taking a ratio of the two separate NC/BC flux ratios, which eliminates the dependency on electron density, the Fe I number density, and the emitting volume. Specifically, this double ratio is given by

$$q = [W_\lambda({\rm NC/BC})_{5616}/W_\lambda({\rm NC/BC})_{4376}] = e^{-(E_{u,\lambda5616}/k - E_{u,\lambda4376}/k)(1/T_{\rm NC} - 1/T_{\rm BC})} ,$$

where $E_{u,\lambda5616}$ and $E_{u,\lambda4376}$ are the energies of the upper levels of λ5616 and λ4376, respectively, and $E_{u,\lambda5616}$ exceeds $E_{u,\lambda4376}$ by 2.7 eV.

Unfortunately, in our data $W_\lambda({\rm NC/BC})_{5616}$ and $W_\lambda({\rm NC/BC})_{4376}$ are not simultaneous ratios. However, these ratios vary by < 40% among all our observing epochs, so their average values will still yield a meaningful estimate of q. The average profile for each of these lines is shown in Figure 16, corresponding to an average value of $W_\lambda({\rm NC/BC})_{4376} = 0.23$ and an average value of $W_\lambda({\rm NC/BC})_{5616} = 0.96$, producing a value of $q = 4.2 \pm 1.7$.

Figure 17 illustrates how $T_{\rm NC}$ and $T_{\rm BC}$ depend on q for this pair of opacity-insensitive lines. Any value of $q > 1$ requires that $T_{\rm NC}$ exceeds $T_{\rm BC}$, which is certainly the case for DR Tau. Identifying the magnitude of the difference in kinetic temperature between the two regions requires a priori knowledge of one of them, however. For example, if $T_{\rm NC}$ is 10^4 K, the corresponding $T_{\rm BC}$ will be ∼6900 K. The result that $T_{\rm NC}$ exceeds $T_{\rm BC}$ is firm, unless the neglect of collisional deexcitation is erroneous. If the NC electron density is sufficiently high that λ4376 becomes collisionally deexcited before

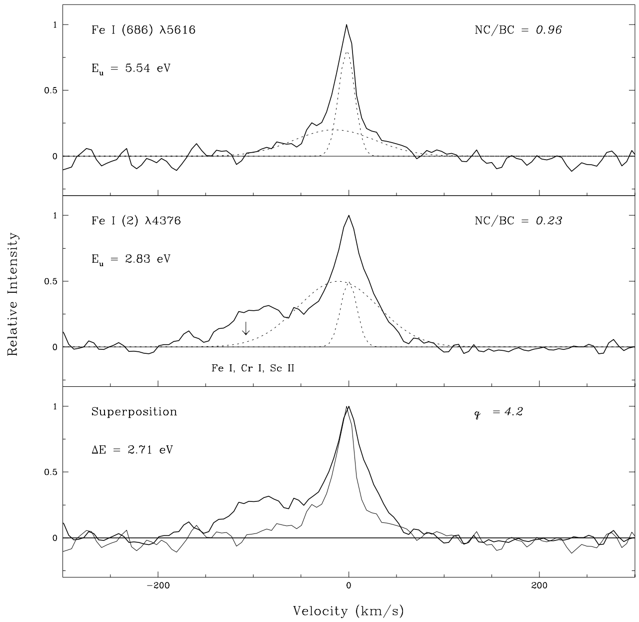

FIG. 16.—Average profiles are shown for the two Fe I lines that are insensitive to opacity (see § 4.3). In the top two panels, the NC and BC fits for each average profile are shown as dashed lines. The lower panel superposes the two average profiles to facilitate their comparison. The temperature sensitive parameter $q = [W_\lambda({\rm NC/BC})_{5616}/W_\lambda({\rm NC/BC})_{4376}] = 4.2$.

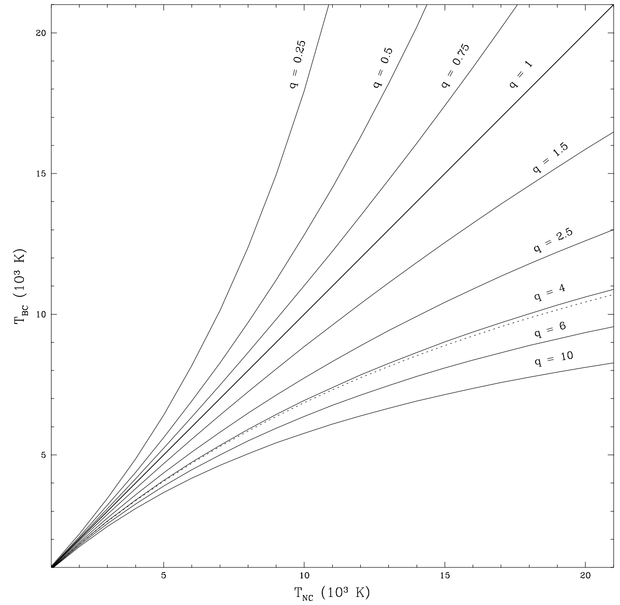

FIG. 17.—Relative values of $T_{\rm NC}$ and $T_{\rm BC}$ are shown for $10 \geq q \geq 0.25$, where $q = [W_\lambda({\rm NC/BC})_{5616}/W_\lambda({\rm NC/BC})_{4376}]$ (see § 4.3). Curves of constant q are plotted at q = 10, 6, 4, 2.5, 1.5, 1, 0.75, 0.5, and 0.25. At $q = 1$, $T_{\rm NC} = T_{\rm BC}$. The observed q of 4.2 ± 1.7, corresponding to the regime where $T_{\rm NC} > T_{\rm BC}$, is shown as a dashed line. For example, if $T_{\rm NC} = 10^4$ K, then $T_{\rm BC} = 6900$ K.

λ5616, then the observed value of q can be reproduced with a smaller difference between $T_{\rm NC}$ and $T_{\rm BC}$, or can even require that $T_{\rm BC} > T_{\rm NC}$.

In summary, we have a rough estimate for the temperature in the NC region of between 8000 K to 14,000 K. We have evidence that the temperatures in the two kinematic regions differ, and that T in the NC region exceeds that in the BC region. While the magnitude of the difference cannot be derived without independent knowledge of the temperature in one of the two regions, the BC temperatures that would follow from the above estimate in the NC region are 5900 to 8500 K.

4.4. *Improving Estimates of Physical Quantities*

The techniques outlined above demonstrate that unblended Fe lines in cTTS spectra can be important diagnostics of opacity, column density, and kinetic temperature. Derivation of these quantities from an LVG analysis requires comparing simultaneous N, T loci from multiple common upper-level line pairs. The sensitivity of this technique depends on (1) maximizing the ratio of A_{ij} between pair members, which enhances the contrast in the line flux ratio between the weak and the strong line, and (2) maximizing the difference in the lower energy level of the stronger line among different pairs. The latter point follows from the fact that the shape and range of an N, T locus from each pair are determined by the column density and temperature required for the stronger line in the pair to become optically thick. Thus comparison of the N, T loci for two line pairs depends on the comparative behavior of the strong line in each pair. A line that decays to a higher lying energy level will become optically thick at a different column density and temperature than a line decaying to an energy level closer to the ground state. Therefore two line pairs with a large difference in the energy of the lower level of the strong line are required to produce distinct N, T loci.

Significant improvements in evaluating column densities and kinetic temperatures from Fe line ratios could be achieved from flux-calibrated spectra covering a broader range of wavelengths than is provided in our data set. In Table 4, we present a list of some of the most suitable common upper level pairs of Fe I and Fe II lines for determining these physical quantities. We include both optical and ultraviolet lines, which allow the greatest contrast in A_{ij} rates and excitation potentials. The selection criteria are (1) an optically thin flux ratio for the pair $F = (A_s/A_w)(\lambda_w/\lambda_s) > 10$; (2) a spontaneous emission rate in the weaker line of a pair $A_w > 10^3\ {\rm s}^{-1}$ for Fe II and $A_w > 10^4\ {\rm s}^{-1}$ for Fe I, which correspond to line equivalent widths ~0.04 Å in DR Tau; and (3) no neighboring lines of comparable or greater strength within ~50 km s^{-1} of line center, as determined from either the optical spectra of DR Tau or the solar UV spectrum. The Fe I and Fe II pairs are ordered by increasing excitation potential of the lower level of the strong line in each pair, which spans ~2.7 eV for Fe I and ~3.2 eV for Fe II. This list of line pairs should provide a starting point for future analysis of Fe lines in cTTS's.

An additional benefit to acquiring UV spectra of cTTS's would be the ability to assess the luminosity radiated by Fe lines, since the strongest transitions are found in this spectral range (see § 5). Indeed, the recent compilation of low-dispersion *IUE* spectra of T Tauri stars by Gomez de Castro & Franqueira (1997) clarifies that Fe II lines are very abundant in the UV spectra of cTTS's.

5. DISCUSSION

From an analysis of the Fe I and Fe II profiles in DR Tau, we have shown that the Fe emission may arise in two distinct kinematic zones. The most compelling argument for this interpretation is that, at each epoch of observation, the NC and BC kinematic properties are each described by a uniform set of parameters, thereby resolving the differences among Fe I and Fe II profiles of different intensities in a self consistent manner. In addition, there are indications that the kinematic distinction between the components is accompanied by physical differences.

The implication of the presence of distinct kinematic zones in the Fe line formation region of cTTS accretion disk

TABLE 4

DESIRABLE COMMON UPPER LEVEL PAIRS

PAIR ORIGIN									
Ion	Term[a]	Multiplet[b]	λ Range[c] (Å)	E_l[d] (eV)	λ_s (Å)	λ_w (Å)	log A_s (s^{-1})	log A_w (s^{-1})	F[e]
Fe I	$z\,^5D^o$	4; 15	3824-3930; 5269-5507	0.05	3856.4	5497.3	6.66	4.80	106
	$y\,^5D^o$	20; 62	3820-3941; 6137-6431	0.96	3878.0	6335.3	6.89	5.15	90
	$z\,^3G^o$	42; 169	4148-4326; 6137-6412	1.49	4202.0	6191.6	6.91	5.69	25
	$y\,^3D^o$	45	3815-3966	1.59	3903.0	3966.1	7.32	6.15	15
	$z\,^5P^o$	60; 106	8327-8824; 8805-10081	2.20	8327.1	8804.6	5.98	4.23	61
	$z\,^5G^o$	168	6319-6669	2.42	6495.0	6593.9	5.89	4.72	15
	$z\,^3G^o$	268	6546-6807	2.75	6592.9	6703.6	5.74	4.18	37
Fe II	$z\,^6P^o$	uv3; 42	2327-2381; 4924-5169	0.05	2332.8	5018.5	8.18	6.43	120
	$z\,^4F^o$	uv35; 37	2331-2392; 4473-4667	0.23	2360.0	4629.3	7.38	5.11	362
	$z\,^6D^o$	uv1; uv32	2586-2631; 2730-2780	0.55	2625.7	2732.4	7.38	4.96	393
	$z\,^6P^o$	uv61; 5	2861-2918; 3316-3426	0.99	2880.8	3425.6	6.34	4.11	201
	$z\,^4D^o$	6	3166-3227	1.70	3210.5	3166.7	6.41	5.15	18
	$z\,^4D^o$	38; 73	4522-4621; 7222-7712	2.86	4508.3	7224.5	6.00	4.40	64
	$z\,^4F^o$	49; 57	5197-5425; 5627-5909	3.31	5234.6	5627.5	5.56	3.18	260

NOTE.—Atomic parameter data are from Kock et al. 1984; Fuhr et al. 1988; Heise & Kock 1990; Bard et al. 1991; O'Brian et al. 1991; Nave et al. 1994; and Giridhar & Arellano Ferro 1995.

[a] Spectroscopic designation of the upper term for each pair.

[b] Parent multiplets of the strong; weak lines in each pair.

[c] Wavelength ranges of the parent multiplets.

[d] Lower level energy of the strong line of each pair.

[e] $F = (A_s/A_w)(\lambda_w/\lambda_s)$; this is the expected flux ratio of the strong to the weak line in the optically thin limit.

systems is not yet clear. Preliminary findings are reported for He I lines in 30 cTTS's (Edwards 1997) where it is demonstrated that the presence of two kinematic components is also an excellent description of these higher excitation lines. In the context of the magnetospheric accretion model, the large linewidths of the BC are compatible with velocities expected in a magnetic funnel flow. The tendency for the BC to be blueshifted, and the fact that redshifted inverse P Cygni absorption below the veiling continuum, just redward of the BC emission, is sometimes seen in our DR Tau spectra in both He I λ5876 and the strongest Fe II lines (see Fig. 1) could be accounted for by a funnel flow origin for this component.

However, as will be clarified in greater detail in the next paper in this series (Beristain et al. 1998), two-component Gaussian fits to the He I lines in DR Tau yield a BC linewidth that is twice the width of that found for Fe I and Fe II, with an FWHM = 232 ± 15 km s^{-1}, and a centroid velocity that has twice the blueshift exhibited by the Fe lines, with a value of -29 ± 9 km s^{-1}. In a funnel flow origin, a factor of 2 difference in BC linewidth between He I and Fe would result if the He I lines are formed in the infalling preshock gas closer to the accretion shock. There, where the free-fall velocity is the highest, the veiling continuum can more easily ionize He and lead to the production of He I lines via recombination and cascade.

The column densities we derive for the Fe BC are also consistent with an origin in the funnel flow. This follows from (1) the finding that Fe II is the dominant ionization state of iron in the BC and (2) the estimate that $N_{\rm Fe\,II} \sim 10^{18}$–$10^{19}$ cm^{-2} for kinetic temperatures in the range 4000–10,000 K. If most of the Fe is assumed to be in Fe II, the corresponding hydrogen column density is then $N_{\rm H} \sim 3 \times 10^{22}$–$3 \times 10^{23}$ cm^{-2}. This compares favorably with column densities expected in a funnel flow geometry in a high accretion rate cTTS. For example, the recent multilevel statistical equilibrium calculations to derive hydrogen line luminosities and profiles in magnetic funnel flows, employing a dipole geometry and a disk truncation radius of several R_* (MCH), have column densities $N_{\rm H} \sim 10^{23}$ cm^{-2} for $\dot{M}_{\rm acc} \sim 10^{-7}$ $M_\odot$ yr^{-1} (J. Muzerolle 1997, personal communication).

However, one problem with the current modeling of the magnetospheric funnel flow is that the source of heating needed to produce the assumed temperature is not specified. This problem is particularly acute if the Fe lines, when the UV transitions are included, constitute a luminosity comparable to that in the hydrogen Balmer lines. The Fe lines pose a problem in that these lines are most probably collisionally excited and therefore require local heating, as opposed to the hydrogen lines that can also be produced by recombination and cascade via utilization of the energy in the photon continuum. We propose here an alternative origin of the Fe BC emission. It is the boundary layer where loading of the gas from the accretion disk onto the field lines of the stellar magnetosphere takes place. The attractive feature of this scenario is that if this coupling region lies well within the corotation radius of the star and disk, dissipation of the gas particle's Keplerian rotational energy before it can corotate with the stellar field line and begin its free fall toward the star produces naturally the heating necessary for collisional excitation of the Fe lines. The evolution in the rotational motion of the gas can also produce the observed BC linewidth.

The heating in such a boundary layer would also produce hydrogen lines. The relative amount of hydrogen versus Fe emission will depend strongly on the equilibrium temperature reached from the balance between the heating and cooling rates. If this temperature is $\lesssim 7000$ K, Fe emission will dominate. Even if the temperature is > 7000 K, however, the hydrogen emission produced in this boundary layer would likely constitute only a fraction of the observed Balmer emission, in view of the presence of other sources of energy, such as the veiling continuum and the heating in the postshock region of the accretion shock. This equilibrium temperature, however, is not likely to be high enough to produce He I lines, and the He I BC would then arise entirely in the preshock gas in the funnel flow.

The dynamics of the gas in this boundary layer may be complicated. The dissipation of the kinetic energy of the gas, allowing some gas to fall toward the star along the stellar magnetic field lines, may also be accompanied by the ejection of other gas particles from this layer as a means of transporting angular momentum outward. This ejection of matter may be a source for the outflow that is later collimated into the jet. For either gas infalling along the stellar magnetic field lines or gas ejected out from the boundary layer, the resulting acceleration outward from the disk could account for the small blueshift observed in the BC of the Fe lines.

We plan to explore this boundary layer scenario further by calculating the excitation of the Fe I and Fe II UV and optical lines in order to evaluate the total cooling rate produced by the two ions and hence obtain an estimate of the minimum heating rate required and to compare this with the hydrogen emission rate. If the luminosity from the Fe lines constitutes a significant fraction of the accretion luminosity, then a boundary layer at the interface between the disk and the stellar magnetosphere may turn out to be an important source of line emission in cTTS's.

The interpretation of the NC is less problematic. Its relatively small linewidth and the fact that it is always observed to be centered on the photospheric velocity suggests that this component is very close to the stellar surface. These kinematic properties would be consistent with either a stellar chromosphere or with emission from the postshock gas after accreting material has arrived at the star. Formation in the postshock gas is favored because the Ca II NC line flux is correlated with the continuum veiling, *r*, among a sample of cTTS's (Batalha et al. 1996). A full study of both the NC and BC emission among a large sample of cTTS's and weak-emission T Tauri stars (wTTS's; Beristain et al. 1998) that lends additional support to this interpretation is in preparation. We also find that this region displays some complexity. For example, in DR Tau, the NC in the He I lines has an FHWM of 48 ± 4 km s^{-1} (see Fig. 1), which is twice as wide as that of the Fe lines. This could be accounted for by a greater turbulence in the higher excitation region closer to the accretion shock.

The possibility that the NC in Fe and He originates in the postshock gas may affect the interpretation of the Balmer lines in cTTS's as well. Although Balmer emission in cTTS's has been well modeled as arising in a funnel flow (HHC; MCH), MCH find that contributions from the accretion shock are also required to account for both the small observed Hβ/Hγ ratios and the Stark-broadened wings at Hα. Our study of the Fe lines in DR Tau suggests that line radiation from the accretion shock will be kinematically distinct, with small linewidths and at rest relative to the star. Indeed, in many cTTS's of low to modest accretion rate, the upper Balmer lines display a profile morphology reminiscent of the Fe lines in DR Tau, with a broad base and a central peak. Further study is needed to determine whether this central peak in the Balmer lines is a signature of the accretion shock or whether it is formed by gas at low projected velocities in the funnel flow, as predicted by the HHC and MCH models.

6. CONCLUSIONS

We analyze 62 unblended Fe I and Fe II emission lines from optical echelle spectra of DR Tau, an extreme cTTS with $\dot{M}_{\rm acc} \sim 10^{-6}\ M_\odot\ {\rm yr}^{-1}$, in order to probe the region where the stellar magnetosphere interacts with the accretion disk. The unblended Fe lines span a range of upper excitation potential from 2.4–5.6 eV in Fe I and from 4.8–5.9 eV in Fe II, with spontaneous transition rates spanning a factor of 10^4 for Fe I and a factor of 600 for Fe II.

Our primary conclusions are:

1. The morphology of the Fe profiles in DR Tau varies systematically with line strength. Line widths increase from a minimum FWHM of ~ 20 km s^{-1} for the weakest lines ($W_\lambda = 0.03$ Å) to a maximum FWHM of 70–90 km s^{-1} for the strongest lines (W_λ from 0.5 to 3.5 Å). The functional form best describing the shape of the line profile evolves from a Gaussian to an exponential form as W_λ increases.

2. The progression of the width and shape of Fe profiles in DR Tau with increasing line strength is best accounted for by differing relative contributions from two Gaussian components. The narrow component (NC) has an FWHM of 22 ± 4 km s^{-1}, comparable to the width of the photospheric Li I line, and is centered on the photospheric velocity. The broad component (BC) has an FWHM of 102 ± 7 km s^{-1} and is frequently blueshifted by up to 10 km s^{-1}. The normalized peak amplitudes of the NC range from 1.0 for the weakest lines to 0.1 for the strongest.

3. Estimates of opacities and column densities are obtained by comparing observed intensity ratios of lines from a common upper level with values expected from a local escape probability calculation. We find that (1) opacities in the NC exceed those in the BC by factors of 2–4 and (2), for the BC, $N_{\rm Fe\,I} \gtrsim 10^{17}$–$10^{18}$ cm^{-2} and $N_{\rm Fe\,II} \gtrsim 10^{18}$–$10^{19}$ cm^{-2} for kinetic temperatures in the range 4000–10,000 K. The corresponding total BC column density is $N_{\rm H} \sim 3 \times 10^{22}$–$3 \times 10^{23}$ cm^{-2}.

4. We estimate the temperature in the Fe NC region to lie between ~ 8400 and 14,000 K, assuming that the size of the emitting region is between $0.2A_*$ and $0.05A_*$. The ratio of NC/BC emission from a pair of Fe I lines that are insensitive to opacity reveals that the kinetic temperature in the NC exceeds that in the BC by several thousand degrees. For example, if $T_{\rm NC} = 10^4$ K, $T_{\rm BC} \sim 7000$ K.

At present, we can only speculate on the relevance of these two kinematic components in accretion disk systems. In the context of a magnetospheric accretion model, the NC is consistent with an origin in the postshock gas close to the stellar surface. In contrast, the BC is likely to be broadened by bulk motion, such as infalling gas in the accretion funnel or rotation in the region coupling the inner disk to the stellar magnetic field.

This paper describes the potential of using Fe lines in cTTS's as diagnostics of the inner accretion zone. To fully utilize these lines requires high-S/N spectrophotometry over as wide a wavelength range as possible. Some of the most promising line pairs for deriving physical parameters require simultaneous optical and ultraviolet coverage, which would provide the largest possible range of Einstein A_{ij} rates between members of a line pair. In addition, the ultraviolet spectrum includes the strongest transitions in both Fe ions and would thereby allow an estimation of the total cooling rate due to Fe, which is expected to be substantial.

We thank David Van Blerkom and Gene Tademaru for helpful discussions and insight in the early stages of this project. Most of the veiling determinations and residual spectra of DR Tau were provided by Pat Hartigan. Lee Hartmann, John Stauffer, and Steve Strom were collaborators in the acquisition of the spectra reported here. S. E. acknowledges support from the National Science Foundation's Faculty Award for Women program.

REFERENCES

Aiad, A., Appenzeller, I., Bertout, C., Isobe, S., Shimizu, M., Stahl, O., Walker, M. F., & Wolf, B. 1984, A&A, 130, 67
Appenzeller, I., Krautter, J., Smolinski, J., & Wolf, B. 1980, A&A, 86, 113
Appenzeller, I., Reitermann, A., & Stahl, O. 1988, PASP, 100, 815
Armitage, P. J., & Clarke, C. J. 1996, MNRAS, 280, 458
Bard, A., Kock, A., & Kock, M. 1991, A&A, 248, 315
Basri, G., & Batalha, C. C. 1990, ApJ, 363, 654
Basri, G., & Bertout, C. 1989, ApJ, 341, 340
Batalha, C. C., Stout-Batalha, N. M., Basri, G., & Terra, M. A. O. 1996, ApJS, 103, 211
Beristain, G., Edwards, S., Kwan, J., & Hartigan, P. 1998, in preparation
Bertout, C. 1989, ARA&A, 27, 351
Bertout, C., Basri, G., & Bouvier, J. 1988, ApJ, 330, 350
Bertout, C., Krautter, J., Möllenhof, C., & Wolf, B. 1977, A&A, 61, 737
Boesgaard, A. M. 1984, AJ, 89, 1635
Bouvier, J., Cabrit, S., Fernández, M., Martín, E. L., & Mathews, J. M. 1993, A&A, 272, 176
Bouvier, J., Covino, E., Kovo, O., Martín, E. L., Mathews, J. M., Terranegra, L., & Beck, S. C. 1995, A&A, 299, 89
Camenzind, M. 1997, in IAU Symp. 182, Herbig Haro Flows and the Birth of Low Mass Stars, ed. B. Reipurth & C. Bertout (Dordrecht: Kluwer), 241
Edwards, S. 1997, in IAU Symp. 182, Herbig Haro Flows and the Birth of Low Mass Stars, ed. B. Reipurth & C. Bertout (Dordrecht: Kluwer), 433
Edwards, S., Hartigan, P., Ghandour, L., & Andrulis, C. 1994, AJ, 108, 1056 (EHGA)
Edwards, S., et al. 1993, AJ, 106, 372
Fuhr, J. R., Martin, G. A., & Wiese, W. L. 1988, J. Phys. Chem. Ref. Data S, 17, 4
Ghosh, P. 1995, MNRAS, 272,763
Giridhar, S., & Arellano Ferro, A. 1995, Rev. Mexicana Astron. Astrofis., 31, 23
Gomez de Castro, A., & Franqueira, M. 1997, *IUE*-ULDA Access Guide No. 8, ESA SP1205
Guenther, E., & Hessman, F. V. 1993, A&A, 268, 192
Hamman, F., & Persson, S. E. 1992, ApJS, 82, 247
Hartigan, P., Edwards, S., & Ghandour, L. 1995, ApJ, 452, 736 (HEG)
Hartmann, L. 1982, ApJS, 48, 109
Hartmann, L., Hewett, R., & Calvet, N. 1994, ApJ, 426, 669 (HHC)
Heise, C., & Kock, M. 1990, A&A, 230, 244
Herbig, G. H. 1962, Adv. Astron. Astrophys., 1, 47
Hessman, F. V., & Guenther, E. 1997, A&A, 321, 497
Hirth, G., Mundt, R., & Solf, J. 1997, A&AS, 126, 437
Isobe, S., Norimoto, Y., & Kitamura, T. 1988, PASJ, 40, 89
Joy, A. H. 1945, ApJ, 102, 168
Kenyon, S. J., et al. 1994, AJ, 107, 2153
Kock, M., Kroll, S., & Schnehage, S. 1984, Phys. Scr., T8, 84
Königl, A. 1991, ApJ, 370, L39
Krautter, J., & Bastian, U. 1980, A&A, 88, L6
Kwan, J. 1997, ApJ, 489, 284
Kwan, J., & Tademaru, E. 1988, ApJ, 332, L41
Lago, M. T. V. T. 1982, MNRAS, 168, 603

Li, J., Wickramasinghe, D., & Ruediger, G. 1996, ApJ, 469, 765
Moore, C. E., Minnaert, M. G. J., & Houtgast, J. 1966, The Solar Spectrum 2935λ to 8770λ, Natl. Bur. Stand. Monogr. 61 (Washington, DC: US GPO)
Mundt, R. 1984, ApJ, 280, 749
Muzerolle, J., Calvet, N., & Hartmann, L. 1998, ApJ, 492, 743 (MCH)
Najita, J., & Shu, F. H. 1994, ApJ, 429, 808
Nave, G., Johansson, S., Learner, R. C. M., Thorne, A. P., & Brault, J. W. 1994, ApJS, 94, 221
O'Brian, T. R., Wickliffe, M. E., Lawler, J. E., Whaling, W., & Brault, J. W. 1991, J. Opt. Soc. Am. B, 8, 1185
Ostriker, E., & Shu, F. 1995, ApJ, 447,813
Paatz, G., & Camenzind, M. 1996, A&A, 308, 77
Safier, P. 1998, ApJ,494, 336
Shu, F. H., Najita, J., Ostriker, E., Wilken, F., Ruden, S., & Lizano, S. 1994, ApJ, 429,781
Smith, K. W., Bonnell, I. A., Lewis, G. F., & Bunclark, P. S. 1997, MNRAS, 289, 151
Willson, L. A. 1974, ApJ, 191, 413
———. 1975, ApJ, 197, 365